Next Materials 7 (2025) 100434

Contents lists available at ScienceDirect

Next Materials

journal homepage: www.sciencedirect.com/journal/next-materials

Research article

Ti_2PTe_2 chalcogenide: A comprehensive DFT study on physical properties

M.H. Mia [a,*], Mst.A. Khatun [b], M. Rahman [c]

[a] Department of Textile Engineering, Northern University Bangladesh, Uttara, Dhaka 1230, Bangladesh
[b] Department of Physics, Hajee Mohammad Danesh Science and Technology University, Dinajpur 5200, Bangladesh
[c] Department of Physics, Uttara University, Uttara-16, Dhaka 1230, Bangladesh

ARTICLE INFO

Keywords:
Ti_2PTe_2 chalcogenide
Density functional theory
Lattice dynamics
Optoelectronics properties
Thermal properties

ABSTRACT

We have investigated the structural, mechanical, lattice dynamics, electronic, optical and thermal properties of Ti_2PTe_2 chalcogenide using density functional theory for the first time. The optimized unit cell parameters show excellent agreement with experimental values. The stability of Ti_2PTe_2 is confirmed by thermodynamic, mechanical, and dynamical stability criteria. The material exhibits softness, machinability, and brittleness, making it suitable for applications requiring ease of fabrication and damage tolerance. The compound is elastically and optically anisotropic. Its electronic properties reveal a metallic nature, characterized by a mix of covalent, ionic, and metallic bonding. Its ultra-low thermal conductivity suggests Ti_2PTe_2 is a promising candidate for thermal barrier coatings (TBCs). Additionally, its strong UV absorption makes it useful for UV detectors, anti-reflective coatings, and protection against photo-disintegration. With a high static refractive index and impressive reflectivity, Ti_2PTe_2 also holds potential for advanced display technologies and solar heating reduction. We believe this study will inspire further research, expanding the material's application potential beyond traditional boundaries.

1. Introduction

Chalcogenide crystals stand out as a distinctive class of materials, fundamentally different from traditional semiconductors or metallic alloys. With a tunable bandgap spanning from 0.0 to 3.5 eV, these covalently bonded materials can exist in both amorphous and crystalline forms, offering flexibility in design and functionality [1]. In recent years, transition metal chalcogenides have garnered significant interest from chemists and materials scientists due to their excellent physical and chemical properties. These crystalline materials, consisting of a chalcogen anion and at least one electropositive metal element, are renowned for their appealing electrical characteristics [2]. Notably, they exhibit fascinating phenomena such as charge density wave behaviour, superconductivity, intercalation reactions, and the potential for surface modification using advanced scanning probe microscopy techniques [3,4]. This versatility translates into a broad spectrum of applications, from solar cells and hydrogen evolution to photocatalytic degradation and lithium-ion batteries [5]. The excellent stability and optoelectronic properties of chalcogenides make them a critical component in advancing these technologies, solidifying their role as a key material in the future of science and engineering.

Ternary metal chalcogenides have emerged as a promising class of metal chalcogenides, primarily due to their low production costs and the abundance of key raw materials [6]. Binary metal chalcogenide like FeS_2, Sb_2S_3, CoS, Cu_2S, NiS, ZnS, Bi_2S_3, and CdS are widely used for their thermoelectric properties, low cost, and reduced toxicity [7]. Recently, compounds such as Sb_2S_3, Sb_2Se_3, Bi_2Te_3, Sb_2Te_3, SnS, SnSe, CdSe, CdTe, ZnSe, and ZnTe have garnered attention for their expanding roles in electrical, optical, switching, photovoltaic, and solar cell applications, highlighting their versatility and growing significance in advanced technologies [8–10]. Of particular interest are tellurium-based chalcopyrite ternary compounds, which boast remarkable optical properties, including transparency in the infrared region and high nonlinear sensitivity [11]. These materials, such as Al_2ZnTe_4, $CuIn_3Te_5$, $CuIn_3Se_5$, $CuGa_3Te_5$ and $ZnIn_2Te_4$, have proven to be pivotal in enhancing solar cell efficiency [11]. Ternary metal chalcogenides (TMCs) have also attracted considerable interest among researchers due to their unique features, which are not achievable with binary chalcogenides. For example, Cu_2SnS_3 and Cu_2SnSe_3 have emerged as promising materials for high-efficiency solar cells [12,13]. Furthermore, ternary transition metal have emerged as promising candidates for counter electrodes (CEs) in various technologies, showcasing impressive device

* Corresponding author.
E-mail address: mdhasan111.ru@gmail.com (M.H. Mia).

https://doi.org/10.1016/j.nxmate.2024.100434
Received 16 September 2024; Received in revised form 25 October 2024; Accepted 18 November 2024

performances. Notable examples include $NiCo_2S_4$ [14], $MMoS_4$ (M = Co, Ni) [15], Cu_3SnS_4 [16], and $CuInS_2$ [17]. Among these, $CoIn_2S_4$ and $NiIn_2S_4$ have demonstrated significant potential in photocatalysis, optoelectronics, light modulation, and photodetection [18,19]. Despite their promise, these materials have been scarcely explored in the context of dye-sensitized solar cells (DSSCs). Metal-ion batteries (MIBs) are widely used in devices from electronics to grid storage, with the search for high-performance anode materials highlighting two-dimensional (2D) materials due to their excellent electrochemical activity [20,21]. Baoxin *et al.* showed that Ti_2PTe_2 monolayers hold potential as anode materials for sodium-ion batteries (SIBs) [22]. Motivated by these advances, we turn our focus to Ti_2PTe_2, a novel chalcogenide predicted to exhibit fascinating properties. Despite the promising characteristics of many tellurium-based ternary transition metal, Ti_2PTe_2 remains largely unexplored of various property. This oversight presents a significant research opportunity, especially given the critical role that structural, elastic and mechanical, lattice dynamics, electronic, optical and thermal properties play in determining a material's suitability for technological applications. Understanding the mechanical properties of Ti_2PTe_2, such as its elastic constants and moduli, are essential for assessing its practical usability in various engineering applications. Additionally, investigating the band structure of Ti_2PTe_2 will provide insights into its electronic properties, such as conductivity and the nature of its electronic states, which are crucial for applications in electronics and energy storage. The optical properties of Ti_2PTe_2, including dielectric constants, absorptivity, reflectivity, refractivity, loss function, and optical conductivity, are crucial for determining its potential in optoelectronic devices like sensors, light modulators, and solar cells. Our motivation to study Ti_2PTe_2 stems from the need to fill this critical research gap and unlock the material's full potential. By systematically investigating these properties using DFT methods, we aim to provide a comprehensive understanding of Ti_2PTe_2, paving the way for its future application in cutting-edge technologies. This research is not only a step forward in the basic understanding of chalcogenide phases but also holds immense promise for practical innovations in fields ranging from electronics to energy storage and beyond.

2. Methodology

2.1. Computational details

The structural, mechanical, lattice dynamics, electronic and thermal properties of the newly chalcogenide phase, Ti_2PTe_2, were meticulously investigated using first-principles calculations within the framework of density functional theory (DFT). For these calculations, we employed the generalized gradient approximation (GGA) with the Perdew–Burke–Ernzerhof (PBE) [23] functional to account for exchange and correlation effects. All computations were performed using the cambridge serial total energy package (CASTEP) code [24,25]. Specifically, the Te - 5 $s^2 5p^4$, P - 3 $s^2 3p^5$, and Ti - 3 $s^2 3p^6 3d^2 4$ s^2 electronic orbitals were included in the pseudopotential calculations. A finely tuned 18×18×2 *k*-point mesh [26] was chosen to enhance the accuracy of the electronic structure calculations. Additionally, an energy cut-off of 500 eV was applied to ensure precise computational results. Structural optimizations were rigorously conducted, with convergence criteria set to a force threshold of less than 2 meV/Å on each atom, a total energy difference within 10 μeV/atom, a maximum ionic displacement of 1 mÅ, a maximum ionic force of 0.03 eV/Å, and a maximum stress of 0.05 GPa. To determine the elastic constants, the stress-strain method was applied, with stringent convergence criteria: a total energy difference of less than 2.0 μeV/atom, a maximum ionic Hellmann–Feynman force below 6.0 meV/Å, and a maximum ionic displacement not exceeding 0.2 mÅ. The lattice dynamic properties of Ti_2PTe_2, encompassing phonon dispersion and density of states, were computed using 9×9×1 supercell with a 5.0 Å cut-off radius, employing the finite displacement method for precise and reliable results.

2.2. Stability calculations

The thermodynamic stability of Ti_2PTe_2 was rigorously assessed by calculating its formation enthalpy (ΔH_f), which was determined using the equation [27]:

$$\Delta E_f(Ti_2PTe_2)_{fu} = \frac{E_{tot}(Ti_2PTe_2)_{fu} - 2E_s(Ti) - E_s(P) - 2E_s(Te)}{N} \quad (1)$$

where, $E_{tot}(Ti_2PTe_2)_{fu}$ is the total energy of Ti_2PTe_2 per formula unit and $E_s(Ti), E_s(P)$ and $E_s(Te)$ denote the total energy of single atomic elements of Ti, P and Te atoms, respectively and N is the number of atoms per formula unit.

Additionally, the cohesive energy (E_{coh}) was calculated to further evaluate the thermodynamic stability of the structure, using the following expression [28]:

$$E_{coh} = -\frac{E_{tot} - [n_{Ti}E(Ti) + n_PE(P) + n_SE(Te)]}{n_{Ti} + n_P + n_{Te}} \quad (2)$$

Here, E_{tot} represents the total energy of the E(Ti), E(P) and E(Te) correspond to the energies of free Ti, P, and Te atoms, respectively. The terms n_{Ti}, n_P, and n_{Te} denote the number of Ti, P, and Te atoms within the unit cell. A higher cohesive energy signifies greater structural stability.

2.3. Mechanical properties calculations

For hexagonal crystals, the elastic tensor is characterized by five independent constants: C_{11}, C_{12}, C_{13}, C_{33}, and C_{44}. The mechanical stability of the crystal is evaluated using Cauchy-Born criteria, which involve the following conditions [29]:

$$\begin{aligned} &C_{11} - |C_{12}| > 0 \\ &(C_{11} + C_{12})\, C_{33} - 2C_{13}^2 > 0 \\ &C_{44} > 0 \end{aligned} \quad (3)$$

To determine the mechanical properties, we first calculate the bulk and shear moduli using the Voigt–Reuss–Hill (VRH) estimation [30,31]. For hexagonal crystals, the Voigt (B_V) and Reuss (B_R) bulk moduli are given by:

$$\left.\begin{aligned} B_V &= (2C_{11} + 2C_{12} + C_{33} + 4C_{13})/9 \\ \text{and}\quad B_R &= C^2/M \end{aligned}\right\} \quad (4)$$

where, $M = C_{11} + C_{12} + 2C_{33} - 4C_{13}$ and $C^2 = (C_{11} + C_{12})C_{33} - 2C_{13}^2$.

For shear moduli, the Voigt (G_V) and Reuss (G_R) moduli are:

$$\left.\begin{aligned} G_V &= (M + 3C_{11} - 3C_{12} + 12C_{44} + 6C_{66})/30 \\ \text{and}\, G_R &= 15\Big/\left[\frac{18B_V}{C^2} + \frac{6}{(C_{11} - C_{12})} + \frac{6}{C_{44}} + \frac{3}{C_{66}}\right] \end{aligned}\right\} \quad (5)$$

The Hill averaging approach is used to determine the average bulk and shear moduli [32]:

$$\left.\begin{aligned} B &= B_H = (B_R + B_v)/2 \\ \text{and}\, G &= G_H = (G_R + G_v)/2 \end{aligned}\right\} \quad (6)$$

Using the calculated bulk and shear moduli, we derive Young's modulus (Y) and Poisson's ratio (ν) with the following relations [32]:

$$\left.\begin{aligned} Y &= \frac{9GB}{3B + G} \\ \text{and}\, \nu &= \frac{3B - 2G}{2(3B + G)} \end{aligned}\right\} \quad (7)$$

Hardness parameters are computed using [33,34]:

$$\left.\begin{aligned} H_{Chen} &= 2\left[\left(\frac{G}{B}\right)^2 G\right]^{0.585} - 3 \\ \text{and} H_{Miao} &= H_V = \frac{(1-2\nu)Y}{6(1+\nu)} \end{aligned}\right\} \tag{8}$$

The Vickers hardness formula, incorporating both Mulliken bond population analysis and metallic bonding corrections, is expressed as [35]:

$$H_v^{\mu} = 740 \quad (P^{\mu} - \quad P^{\mu'})(\nu_b^{\mu} \quad)^{-\frac{5}{3}} \tag{9}$$

where P^{μ} is the Mulliken bond overlap population of the μ-type bond, $P^{\mu'} = n_{free}/V$ is the metallic population and is estimated from the volume of the unit cell V and the number of free electrons in a unit cell is $n_{free} = \int_{E_p}^{E_F} N(E)dE$, ν_b^{μ} is the volume of μ-type bond, which is determined by the bond length d^{μ}. The number of bonds N_b^{μ} of μ- type per unit volume can be written as $\nu_b^{\mu} = (d^{\mu})^3 / \sum_{\nu}\left[(d^{\mu})^3 N_b^{\mu}\right]$.

The total Vickers hardness for a crystal is given as the geometric average of all bond types:

$$H_v = \left[\prod^{\mu}(H_v^{\mu})^{n^{\mu}}\right]^{1/\sum n^{\mu}} \tag{10}$$

Fracture toughness (K_{IC}) is predicted using the empirical model by Niu *et al.* [36]:

$$K_{IC} = {\alpha_0}^{-1/2} {V_0}^{1/6} [\xi(\nu) Y]^{3/2} \tag{11}$$

where α_0 is an enhancement factor (8840 GPa for covalent and ionic crystals), and $\xi(\nu)$ is a dimensionless parameter [37]:

$$\xi(\nu) = \frac{1 - 13.7\nu + 48.6\nu^2}{1 - 15.2\nu + 70.2\nu^2 - 81.5\nu^3} \tag{12}$$

Elastic anisotropy factors are calculated to evaluate the stiffness constants' impact on the crystal's anisotropy [38]:

1. $A_1 = \frac{4C_{44}}{C_{11}+C_{33}-2C_{13}}$ for {100} shear planes between [011] and [010] directions
2. $A_2 = \frac{4C_{55}}{C_{22}+C_{33}-2C_{23}}$ for {010} shear planes between [101] and [001] directions
3. $A_3 = \frac{4C_{66}}{C_{11}+C_{22}-2C_{12}}$ for {001} shear planes between [110] and [010] directions

In an isotropic crystal, all A_i (i = 1–3) values would be equal to 1.

2.4. Lattice dynamic calculations

The Debye temperature is calculated using Boltzmann's constant (k_B), Planck's constant (h), and number of atoms per unit cell (n), and optimized volume V_0 by the relation [39]:

$$\Theta_D = \frac{h}{k_B}\left[\frac{3n}{4\pi V_0}\right]^{1/3} \nu_a \tag{13}$$

The average sound velocity (ν_a) is determined by [39]:

$$\nu_a = \left[\frac{1}{3}\left(\frac{2}{{\nu_t}^3} + \frac{1}{{\nu_l}^3}\right)\right]^{-1/3} \tag{14}$$

The longitudinal (ν_l) and transverse (ν_t) sound velocities are derived using Navier's equation [39], which incorporates the material's shear modulus (G), bulk modulus (B), and density (ρ):

$$\left.\begin{aligned} \nu_l &= \left(\frac{3B + 4G}{3\rho}\right)^{\frac{1}{2}} \\ \text{and} \nu_t &= \left(\frac{G}{\rho}\right)^{1/2} \end{aligned}\right\} \tag{15}$$

The melting temperature (T_m) of the materials is estimated using an empirical formula based on their elastic constants [40]:

$$T_m = 354K + \left(\frac{4.5K}{GPa}\right)\left(\frac{2C_{11} + C_{33}}{3}\right) \pm 300 \quad K \tag{16}$$

This relationship provides a practical means of predicting T_m from the elastic properties of the material.

The lattice thermal conductivity (κ_{ph}) is calculated using Slack's formula, which incorporates several material-specific parameters [41]:

$$\kappa_{ph} = A(\gamma)\frac{M_{av}{\theta_D}^3 \delta}{\gamma^2 n^{2/3} T} \tag{17}$$

Here, M_{av} is the average atomic mass (in kg/mol), δ is the cubic root of the average atomic volume, n is the number of atoms per unit cell, T is the absolute temperature, γ is the Grüneisen parameter derived from Poisson's ratio (ν), and A is a factor (in W-mol/kg/m^2/K^3) dependent on γ. The Grüneisen parameter, γ, which addresses phonon-phonon interaction anharmonicity, can be calculated as [42]:

$$\gamma = \frac{9\left(\nu_l^2 - \frac{4}{3}\nu_t^2\right)}{2\left(\nu_l^2 - 2\nu_t^2\right)} = \frac{3(1+\nu)}{2(2-3\nu)} \tag{18}$$

The coefficient $A(\gamma)$ in Slack's model is determined by Julian's equation [43]:

$$A(\gamma) = \frac{5.720 \times 10^7 \times 0.849}{2 \times (1 - 0.514/\gamma + 0.228/\gamma^2)} \tag{19}$$

The minimum thermal conductivity ($k_{\min}$) is evaluated using Clark's formula [44], which offers insight into the material's behaviour at low temperatures:

$$k_{\min} = k_B \nu_a \Lambda_{\min} = k_B \nu_a \left(\frac{M}{n\rho N_A}\right)^{-2/3} \tag{20}$$

where, $\Lambda_{\min}$ is the phonon mean free path, M is the molecular mass, ρ is the density of the crystal, and N_A is Avogadro's constant.

2.5. Optical constant calculations

To understand the interaction of materials with light, we extract key optical parameters from the complex dielectric function, given by:

$$\varepsilon(\omega) = \varepsilon_1(\omega) + i\varepsilon_2(\omega) \tag{21}$$

Here, the real part $\varepsilon_1(\omega)$ corresponds to the degree of polarization, while the imaginary part $\varepsilon_2(\omega)$ is associated with the material's absorption of radiation.

The real part $\varepsilon_1(\omega)$ can be computed using the Kramers–Kronig relation [45]:

$$\varepsilon_1(\omega) = 1 + \frac{2}{\pi} P \int_0^{\infty} \frac{\omega' \varepsilon_2(\omega')}{\omega'^2 - \omega^2} d\omega' \tag{22}$$

where P denotes the principal value of the integral. This relationship provides insight into the material's polarization response.

The imaginary part $\varepsilon_2(\omega)$ can be derived from the momentum matrix elements by considering electronic transitions between occupied and unoccupied states [46]:

$$\varepsilon_2(\omega) = \frac{2e^2\pi}{\Omega\varepsilon_0} \sum_{k,\ \nu\ ,c} \left|\psi_k^c \left| u.r \right| \psi_k^v\right|^2 \delta\left(E_k^c - E_k^v - E\right) \quad (23)$$

where $\boldsymbol{u}$ represents the polarization of the incident electric field, e is the electronic charge, and Ω is the unit cell volume. The functions ψ_k^v and ψ_k^c denote the wave functions of the valence and conduction bands at wavevector k, respectively.

The refractive index, $n(\omega)$, quantifying the bending of light within the material, is computed using [47,48]:

$$n(\omega) = \left[\sqrt{\varepsilon_1^2(\omega) + \varepsilon_2^2(\omega)} + \varepsilon_1(\omega)\right]^{1/2} \Big/ \sqrt{2} \quad (24)$$

The absorption coefficient, $\alpha(\omega)$, indicating the rate at which light diminishes as it penetrates the material, is calculated by [47,48]:

$$\alpha(\omega) = \sqrt{2}\omega\left[\sqrt{\varepsilon_1^2(\omega) + \varepsilon_2^2(\omega)} - \varepsilon_1(\omega)\right]^{1/2} \quad (25)$$

Optical conductivity, $\sigma(\omega)$, describes the material's capacity to conduct electrons under varying photon energies and is given by [47,48]:

$$\sigma(\omega) = \frac{\omega\varepsilon_2}{4\pi} \quad (26)$$

Reflectivity, $R(\omega)$, measures the fraction of incident light reflected off the material's surface, and is determined by [47,48]:

$$R(\omega) = \left|\frac{(\varepsilon(\omega)^{1/2} - 1)}{(\varepsilon(\omega)^{1/2} + 1)}\right|^2 \quad (27)$$

Finally, the loss function, $L(\omega)$, describing the energy loss experienced by fast electrons traversing the material, is expressed as [49]:

$$L(\omega) = \frac{\varepsilon_2(\omega)}{\varepsilon_1^2(\omega) + \varepsilon_2^2(\omega)} \quad (28)$$

3. Outcomes and analysis

3.1. Crystal structure and stability

Motivated by the intriguing electronic, optical, and mechanical properties of tellurium-based chalcogenides, we focus on the Ti_2PTe_2 compound, due to its potential for advanced applications such as metal-ion batteries and photovoltaics [22]. Ti_2PTe_2 crystallizes in a hexagonal $R\bar{3}m$ space group (No. 166), as illustrated in Fig. 1. Prior to determining lattice constants, atomic positions were optimized via total energy and force minimization using Broyden's method [50,51] (see Table 1), ensuring precise structural analysis. Table 1 presents a GGA-optimized atomic positions to theoretical values for each element. By calculating total energy across various volumes and applying the Murnaghan equation of state [52], we determined the unit cell's lattice parameters at the lowest energy. Following geometric relaxation, the physical properties of Ti_2PTe_2 were computed, with relaxed cell parameters compared to previous experimental results [53]. The close agreement between our calculated lattice parameters and existing data confirms the reliability and accuracy of our study (see Table 2). In Ti_2PTe_2, the Te-Ti bond length is 2.79 Å, while the P-Ti bond length is 2.48 Å. The P-Ti bond is stronger compared to the Te-Ti bond (see Table 6). This difference is influenced by the atomic radius of the elements involved. As the atomic radius increases, it expands the atomic volume, impacting crystal packing and bond strength within the lattice.

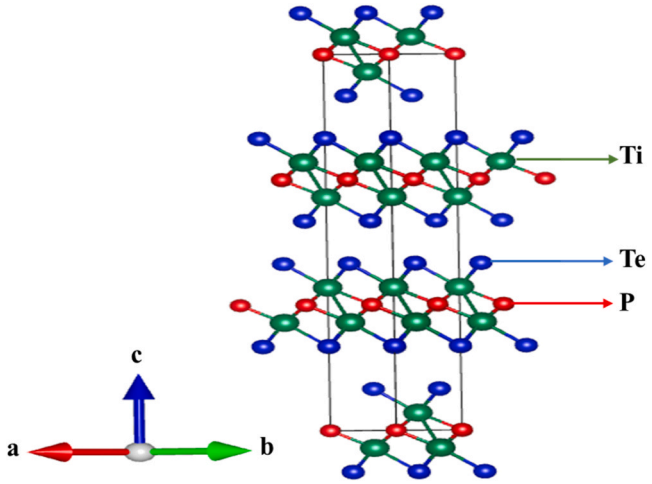

Fig. 1. Schematic representation unit cell structure of Ti_2PTe_2 chalcogenide.

As Ti_2PTe_2 chalcogenide has yet to be experimentally synthesized [54], assessing its stability is crucial before exploring its properties and potential applications. The thermodynamic stability of Ti_2PTe_2 was assessed using formation enthalpy (ΔH_f), cohesive energy (E_{coh}), and ground state energy (E). The results are summarized in Table 2. The negative values for formation enthalpy, cohesive energy, and ground state energy indicate strong thermodynamic stability for Ti_2PTe_2. This stability supports its potential for further study.

3.2. Elastic and mechanical properties

Elastic properties are of paramount importance for understanding the mechanical behavior of materials, particularly in assessing their response to stress, deformation, and recovery. These properties are critical for unveiling insights into the binding characteristics between atomic planes, the nature of anisotropy in bonding, and the overall structural stability. Key elastic parameters like stiffness, strength, elastic moduli, hardness, ductility/brittleness, and machinability offer a comprehensive understanding of how materials perform under mechanical stress. In the case of Ti_2PTe_2 chalcogenide, we explore these elastic characteristics to reveal its mechanical behavior for the first time. In hexagonal chalcogenide crystals, the unique structure determines the number of independent elastic constants, with five key constants (C_{11}, C_{12}, C_{13}, C_{33}, and C_{44}) playing a crucial role in defining the mechanical properties. The mechanical stability of such materials is evaluated using the Born stability criteria, as detailed in Eq. 3. Our study, as presented in Table 3, includes a comprehensive analysis of Ti_2PTe_2 alongside with other ternary tellurium-based chalcogenide compounds. The calculated elastic constants for Ti_2PTe_2 satisfy the Born stability criteria, confirming its mechanical stability. Notably, while there is a lack of experimental or theoretical data for elastic constants of Ti_2PTe_2, a comparison with reported data for other ternary tellurium-based chalcogenides [55,56] shows a good agreement which highlights the reliability and accuracy of our computational approach (see Fig. 2**(a)**). According to Fig. 2 **(a)**, Ti_2PTe_2 exhibits higher stiffness along the a-axis (C_{11}) and greater softness along the c-axis (C_{33}), compared to other chalcogenides. Its lower shear resistance (C_{44}) offers a balance of rigidity and flexibility, making it promising for advanced applications.

Again, Table 3 reveals that the estimated values of C_{11} and C_{33} are significantly higher than the other elastic constants, suggesting that Ti_2PTe_2 is more resistant to uniaxial stress along both the a (ϵ_{11}) and c (ϵ_{33}) axes. Notably, the larger value of C_{11} compared to C_{33}, indicates that the c-axis is more compressible than the a-axis. The lower value of C_{44}, essential for the shear modulus, suggests that Ti_2PTe_2 may undergo shear deformation more easily than uniaxial compression. The difference between C_{11} and C_{33} highlights the material's elastic anisotropy, with a larger difference indicating greater anisotropy. Additionally, C_{12} and C_{13} represent off-diagonal shear components, further affecting the mechanical behavior of Ti_2PTe_2 by influencing stress distribution along the crystallographic axes. The relationship $C_{12} + C_{11} > C_{33}$ implies that the bonding strength and tensile elastic modulus in the (001) plane surpass those along the c-axis. The tetragonal shear modulus, C_t =

Table 1
The crystallographic data for Ti_2PTe_2 structure: detailed coordinates (x, y, z) and equivalent positions (N_{eq}) employed in computational analysis.

Structure	Space group	Formula unit	Equivalent sites	N_{eq}	Wyckoff notations	(x, y, z)
Ti_2PTe_2	$R\bar{3}m$ (no. 166)	3	Ti	6	c	(0, 0, 0.37975)
			P	3	a	(0, 0, 0)
			S	6	c	(0, 0, 0.77669)

Table 2
The comprehensive overview of lattice dimensions (a, c, and V in Å, Å, and Å^3) and stability indicators (ΔH_f, E_{coh}, and E in eV/atom, eV/atom, and eV) of Ti_2PTe_2 structure.

Structure	Lattice dimensions			Stability indicators			Ref.
	a	c	V	ΔH_f	E_{coh}	E	
Ti_2PTe_2	3.64	29.94	343.84	−1.11	−6.02	−11844.1	This work
	3.64	28.49	-	-	-	-	[53]

$\frac{C_{11}-C_{12}}{2}$, reflects a material's dynamical stability [57,58]. Large positive values of C_t (C_t= 46.94 GPa) indicate strong stability and a high sound velocity for transverse waves.

The Kleinman parameter (ζ) is a key measure of a crystal's stability, reflecting its response to internal strain. Defined by the formula [59] $\zeta = \frac{C_{11}+8C_{12}}{7C_{11}+2C_{12}}$, this dimensionless parameter typically ranges from 0 to 1. A value near 0 indicates that the crystal's resistance to external stresses is primarily driven by bond bending, while a value near 1 suggests stretching or contracting is the dominant factor. For Ti_2PTe_2, the calculated Kleinman parameter of 0.44 suggests a balanced interplay between bond bending and stretching, highlighting its structural adaptability.

The elastic moduli of Ti_2PTe_2, key indicators of its macroscopic mechanical properties, were calculated from the estimated elastic constants and are summarized in Table 3. Using the Voigt-Reuss-Hill (VRH) approximation [30,31] (see Eqs. 4–7 from Section 2.3), we determined these values for the hexagonal crystal structure. Notably, no experimental or theoretical data on the elastic moduli of Ti_2PTe_2 currently exist. However, our computed moduli closely align with values reported for other ternary tellurium-based chalcogenides [55,56], as shown in Fig. 2**(b)**. However, Ti_2PTe_2 exhibits excellent mechanical properties among the listed compounds in Table 3, demonstrating notable strength and stiffness.

The bulk and shear moduli are crucial for assessing a material's mechanical performance. The bulk modulus (B) is a key indicator of the strength of inter-atomic bonds and a material's ability to resist changes in volume, encapsulating its resistance to compression and deformation. A high bulk modulus signifies robust inter-atomic bonding, translating to enhanced durability against both volume and plastic deformation. Ti_2PTe_2, as shown in Fig. 2**(b)**, exhibits a notably higher bulk modulus compared to other materials in Table 3, underscoring its greater resistance to compression and making it suitable candidate for industrial applications. The trend of the calculated bulk modulus follows the order: Ti_2PTe_2> $CuInTe_2$> Cu_2SnTe_3> $AgInTe_2$> $LiGaTe_2$, positioning Ti_2PTe_2 as the least compressible material in this group. This suggests that Ti_2PTe_2, with its stiffer lattice, is more resistant to volume deformation than its counterparts. Furthermore, its larger bulk modulus, especially when compared to other chalcogenide phases in Table 3, points to the greater strength of the chemical bonds within the Ti_2PTe_2 structure. Similarly, the shear modulus (G) serves as a critical metric for assessing a material's ability to resist plastic deformation, essentially measuring its capacity to withstand shape changes. This property is closely tied to both the material's hardness and the elastic constant C_{44}. A higher shear modulus signifies a stiffer, harder material, while a lower value indicates softness and greater susceptibility to deformation. In the case of Ti_2PTe_2, its shear modulus is higher than that of other materials listed in Table 3 (Ti_2PTe_2> $CuInTe_2$> Cu_2SnTe_3> $AgInTe_2$> $LiGaTe_2$), showcasing its greater hardness and resistance to deformation. Furthermore, the fact that B>G for Ti_2PTe_2 reveals that its mechanical stability is more dependent on its resistance to shear than to compression. This reinforces its suitability for advanced engineering applications where resilience to

Table 3
The single crystal elastic constants (C_{ij} in GPa) and polycrystalline elastic moduli (B, G, Y in GPa) for Ti_2PTe_2 with other available value.

Compounds	C_{11}	C_{33}	C_{44}	C_{12}	C_{13}	B	G	Y	Ref.
Ti_2PTe_2	131.45	44.23	20.73	37.61	27.25	47.47	27.47	69.09	This work
$LiGaTe_2$	38.60	39.70	18.90	17.60	22.80	26.93	13.10	33.82	[55]
$AgInTe_2$	48.07	47.94	20.22	31.16	31.71	36.76	14.00	37.28	[56]
$CuInTe_2$	65.32	56.60	40.94	37.86	35.74	43.21	25.64	64.22	[56]
Cu_2SnTe_3	74.73	56.34	26.64	22.48	31.29	42.16	19.21	50.04	[56]

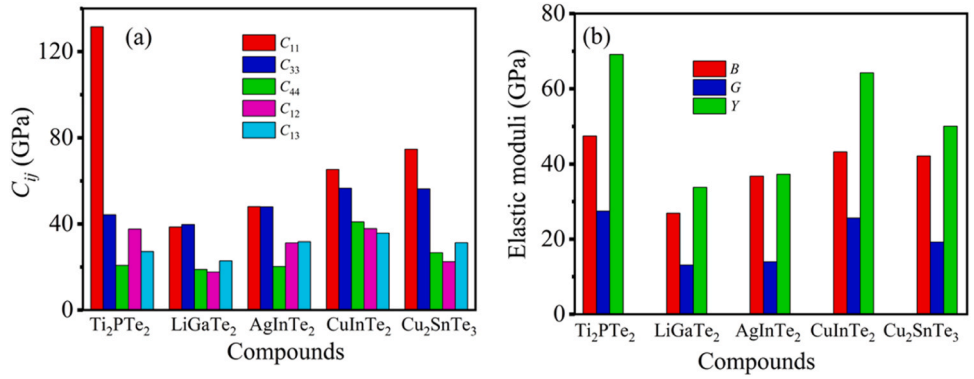

Fig. 2. The comparison of Ti_2PTe_2's elastic properties (constants and moduli) with different chalcogenides.

both stress and deformation is essential, positioning Ti_2PTe_2 as applicable material for cutting-edge technologies.

In materials science, the relationship between the bulk modulus (B) and the shear modulus (G) helps reveal the nature of the chemical bonding within a material. For covalent materials, the typical relation is $G \approx 1.1B$, reflecting strong directional bonds, while for ionic materials, the ratio is generally $G \approx 0.6B$, highlighting more non-directional bonding[60]. In the case of Ti_2PTe_2, the calculated ratio of $G/B = 0.578$ (using the Voigt, Reuss, and Hill averaging methods) closely aligns with the ratio expected for ionic materials. This suggests that ionic bonding plays a dominant role in the structural stability of Ti_2PTe_2 under ambient conditions.

Young's modulus (Y) is crucial for predicting how a material behaves under tensile force, as it directly relates to stiffness. A higher Y indicates greater resistance to deformation, suggesting a stiffer and more covalent material. Additionally, Young's modulus (Y) is inversely related to thermal shock resistance (R), making it a critical factor in determining material durability. The thermal shock resistance can be calculated using the formula[61,62] $R = \frac{\sigma_b(1-\nu)}{\alpha Y}$, where σ_b is strength and α is the thermal expansion coefficient. A lower Young's modulus (Y) leads to improved thermal shock resistance, assuming material strength remains consistent. This makes a low Y advantageous for applications requiring high resistance to rapid temperature changes. The Young's modulus of Ti_2PTe_2 (69.09 GPa) is significantly lower compared to other MAB phases, such as Mo_2AlB_2 (312 GPa), M_2AB_2 (Where M = Hf, Zr; A=Ga, Ge) (250–292 GPa), and Cr_2AlB_2 (397 GPa)[63–65]. This lower Y value suggests that Ti_2PTe_2 could offer excellent thermal shock resistance compared to other MAB materials, provided its strength is well-controlled. With its notably low Young's modulus, Ti_2PTe_2 demonstrates excellent potential for enhanced thermal shock resistance. This makes it a strong candidate for applications such as thermal barrier coatings.

The lattice thermal conductivity (k_{ph}) is strongly linked to Young's modulus (Y) ($k_{ph} \approx \sqrt{Y}$) because both properties are influenced by the material's atomic bonding and structure[66,67]. Materials with a high Young's modulus typically have strong atomic bonds, which can lead to higher phonon velocities. Phonons, which are the primary carriers of heat in non-metallic solids, propagate more efficiently in materials with stiffer atomic structures, resulting in higher lattice thermal conductivity. Conversely, materials with a lower Y value tend to have weaker atomic bonds, leading to lower phonon velocities and increased phonon scattering. This reduces the efficiency of heat transfer, lowering the lattice thermal conductivity. Therefore, a lower Y not only improves thermal shock resistance but can also contribute to a reduction in thermal conductivity, which is advantageous for applications like thermal barrier coatings, where minimizing heat transfer is important.

The mechanical properties of materials are crucial in determining their suitability for various applications, with brittleness and ductility playing key roles in material performance. Poisson's ratio (ν) and Pugh's ratio (G/B) are widely used to assess these traits. According to Frantsevich *et al.* [68], materials with $\nu < 0.26$ are classified as brittle, while those with $\nu > 0.26$ are ductile. For Ti_2PTe_2, the calculated Poisson's ratio is 0.25, which places it in the brittle category. Similarly, Pugh's ratio [69] (G/B) indicates ductility if the value below 0.571; otherwise, the material is brittle. The calculated G/B ratio of 0.578 for Ti_2PTe_2 confirms that this material is brittle. In comparison, the well-known brittle ceramic materials SiC (G/B: 0.85)[70] and ZrC (G/B: 0.76)[71] demonstrate significantly higher resistance to shear deformation. Even the damage-tolerant layered ternary carbides and nitrides, such as Ti_3SiC_2 (G/B: 0.65) and Hf_3AlN (G/B: 0.67)[72], which are recognized for their robustness, exhibit higher Pugh's ratios. In contrast, Ti_2PTe_2 has a notably lower G/B ratio, underscoring its reduced shear resistance and intrinsic brittleness. This brittleness could be a manageable trait, emphasizing the importance of aligning material properties with specific design needs.

Poisson's ratio (ν) provides valuable insights into the nature of interatomic forces and chemical bonding in solids. If ν falls within the range of 0.25–0.50, it typically indicates that central forces dominate the interatomic interactions[73]. For Ti_2PTe_2, with a Poisson's ratio of 0.25, it suggests that the material's phases are primarily governed by effective central forces. Additionally, Poisson's ratio helps predict the type of chemical bonding. A material with $\nu = 1.0$ is considered fully covalent, while $\nu = 0.33$ suggests metallic bonding[74]. Since the Poisson's ratio of Ti_2PTe_2 is 0.25, it indicates that the material exhibits a blend of covalent and metallic bonding characteristics. This mixture enhances the versatility of Ti_2PTe_2, potentially contributing to a balance between structural rigidity and electronic properties, which makes it suitable for a range of applications where such dual properties are desired.

The hardness of a material, while not directly measured by its elastic moduli, can often be predicted by understanding key factors like the bulk modulus (B), shear modulus (G), and Young's modulus (Y). These moduli provide insight into how a material resists various types of deformation. Hardness, a vital property for resisting permanent deformation, is crucial for industrial applications like optoelectronics, microelectronics, and heavy-duty products. Hard materials (hardness > 10 GPa) are ideal for cutting tools and wear-resistant coatings, while softer materials (hardness < 10 GPa) are more suited for machinable and damage-tolerant purposes [75]. The calculated hardness values for Ti_2PTe_2, using Chen's (4.32 GPa) and Miao's (4.61 GPa) formulas, indicate it falls into the soft material category. This softness suggests Ti_2PTe_2 is highly machinable and suitable for applications requiring ease of fabrication and damage tolerance, making it an excellent candidate for industrial uses where such characteristics are desirable. The machinability of materials can be assessed using the bulk modulus (B) and shear constant (C_{44}), where a higher B/C_{44} ratio indicates better lubrication, reduced friction, and increased plasticity. Ti_2PTe_2, with its high bulk modulus and low shear resistance, demonstrates excellent machinability, making it ideal for applications requiring easy processing and enhanced deformation capabilities.

In this study, we delve into the elastic anisotropy of Ti_2PTe_2, key to understanding its performance under diverse conditions. Elastic anisotropy plays a crucial role in defining the mechanical behavior of materials, affecting processes such as plastic deformation, crack propagation, and stress tolerance[76]. Looking back at the crystal structure [Fig. 1], it is evident that the atomic arrangements along the $a(b)$ and c directions differ significantly. This variation in atomic positioning results in distinct bond strengths along these directions. For instance, the bond strength in the $a(b)$ direction is represented by C_{11}, while that in the c direction is denoted by C_{33}. The inequality $C_{11} \neq C_{33}$ highlights this anisotropy, reflecting the non-uniform distribution of mechanical properties across different crystallographic axes. Various experimental and theoretical metrics have been developed to estimate elastic anisotropy in crystals. Four widely used methods include shear anisotropy factors, the universal anisotropy index, linear compressibility coefficients, and 3D representations[77]. To assess Ti_2PTe_2's elastic anisotropy, these techniques were applied, offering a comprehensive understanding of its directional mechanical properties and the degree of anisotropy.

One of the key tools used to measure this anisotropy is the shear anisotropic factor, which quantifies how mechanical properties, particularly shear modulus, vary in different crystallographic planes. For Ti_2PTe_2, our calculations of the shear anisotropy factors offer important insights into its directional mechanical properties. The shear anisotropic factor consists of three components: A_1, A_2, and A_3, corresponding to the {100}, {010}, and {001} crystallographic planes, respectively. These indices help evaluate how the material resists shear stress in these specific directions. In an isotropic material, where the properties are uniform in all directions, these factors would equal 1. However, for Ti_2PTe_2, the values of A_1 and A_2 deviate from unity (refer to Table 4), indicating significant anisotropy in these planes. This means the shear modulus, and thus the material's resistance to deformation, varies depending on

the direction of the applied stress. Such anisotropy impacts how Ti_2PTe_2 behaves under mechanical loads, potentially influencing its ability to withstand plastic deformation and crack growth along these planes. The fact that $A_3 = 1$ suggests isotropic behavior in the {001} plane, indicating that the material exhibits uniform mechanical properties in this direction. This balanced behavior in the {001} plane could contribute to predictable performance in applications where stresses are applied perpendicular to this plane.

The universal anisotropy index ($A^U = \frac{B_V}{B_R} + 5\frac{G_V}{G_R} - 6 \geq 0$), introduced by Ranganathan and Ostoja-Starzewsky [78], offers a comprehensive measure of a crystal's elastic anisotropy A value of zero represents perfect isotropy, while positive values reflect increasing anisotropy. For Ti_2PTe_2, the calculated A^U value of 2.33 highlights significant anisotropy, confirming its distinct elastic behavior. This indicates that the mechanical response of Ti_2PTe_2 varies substantially depending on the direction of the applied stress. The A^U anisotropy parameter not only confirms the anisotropic nature of Ti_2PTe_2 but also provides valuable insights into its mechanical stability and directional behavior under stress. This understanding allows for more informed material design and optimization, ensuring reliable performance in advanced engineering applications where mechanical anisotropy can be both a challenge and an opportunity for enhanced performance.

In hexagonal crystals like Ti_2PTe_2, anisotropy can be quantified by the linear compressibility coefficients [79], expressed as k_c/k_a ($k_c/k_a = \frac{C_{11}+C_{12}-2C_{13}}{C_{33}-C_{13}}$). Here, k_c and k_a represent the compressibility along the *c*- and *a*-axis, respectively. Values of k_c/k_a less than 1 indicate smaller compressibility along the *c*-axis compared to the *a*-axis, and vice versa. However, the calculated ratio of 6.75 for Ti_2PTe_2 reveals the compressibility is significantly higher along the *c*-axis, highlighting a pronounced anisotropy in its mechanical behavior. This pronounced anisotropy means that under stress, Ti_2PTe_2 will deform much more readily in the *c*-direction, which can affect its mechanical stability and deformation behavior under load. Understanding this behavior is crucial for designing components where directional strength and stress distribution are essential. Similar anisotropic trends have been reported in other MAX and MAB phases[80–82].

We also investigated the directional anisotropy of Ti_2PTe_2 in terms of Young's modulus (Y), shear modulus (G), linear compressibility (β), and Poisson's ratio (ν) using the ELATE software [83]. ELATE, an open-source tool, provides 2D and 3D visualizations of elastic anisotropy, enabling direct insight into these mechanical properties. Isotropic materials display uniform, circular 2D and spherical 3D representations, whereas deviations indicate anisotropy. The 2D projections of Ti_2PTe_2's elastic properties (Y, β, G, and ν) in the xy, xz, and yz planes (see Fig. 3 **(a-d)**) clearly demonstrate its anisotropic nature. The greater the deviation from a perfect round shape in these plots, the higher the level of anisotropy in the respective plane, highlighting the material's elastic behavior.

To analyze the mechanical anisotropy of Ti_2PTe_2, we further computed the maximum and minimum values of Y, β G, and ν using the ELATE code, as detailed in Table 5. These calculations confirm that Ti_2PTe_2 exhibits significant anisotropy across all elastic properties. Additionally, the anisotropy A_X for each modulus X is defined as:

$$A_X = \begin{cases} X_{\max}/X_{\min} & \text{if sign } (X_{\max}) = \text{sign } (X_{\max}) \\ \infty & \textit{otherwise} \end{cases}$$

As shown in Table 5, Ti_2PTe_2 exhibits notable anisotropy in Y and β, while the shear modulus ($A_G = 3.2$) shows the lowest anisotropy, indicating more uniform shear resistance. Poisson's ratio, with $A_\nu = \infty$, reflects the most pronounced directional dependence.

3.3. Vickers hardness and Mulliken bond population

Hardness, a crucial property of solids, indicates their resistance to deformation, indentation, and wear. In this study, we assessed the bonding characteristics of Ti_2PTe_2 by calculating its Vickers hardness using Mulliken bond population analysis (see Eqs. 9 and 10 in Section 2.3). Due to the delocalization of metallic bonding, a direct correlation between hardness and metallic bonds is not typically observed. However, Gao *et al.* [35] adapted this methodology to account for compounds with partial metallic bonding. The Vickers hardness of Ti_2PTe_2 is calculated as 2.96 GPa (see Table 6), which is consistent with the range of MAX phase compounds (2–8 GPa) [84]. This value suggests that Ti_2PTe_2 is soft and easily machinable, making it a promising material for applications requiring such properties. The relatively low hardness of Ti_2PTe_2 compared to other materials like Hf_2InB_2 (3.91 GPa), Hf_2SnB_2 (4.41 GPa), and Ti_2InB_2 (4.05 GPa), highlights its softness and machinability[80,81]. This characteristic makes Ti_2PTe_2 suitable for specific applications that benefit from its ability to be easily processed and shaped without causing significant wear to tools or equipment. The Mulliken bond population data, as presented in Table 6, highlight the bond overlap populations and bond lengths for Ti_2PTe_2. Positive bond overlap values signify bonding interactions, while negative values reflect antibonding interactions [85]. For hexagonal Ti_2PTe_2, both types of interactions are present, with the P–Ti bond displaying bonding characteristics and the Te–Ti bond exhibiting an antibonding nature. This coexistence of bonding and antibonding interactions in Ti_2PTe_2 further elucidates its mechanical behavior, supporting its classification as a soft material with good machinability.

3.4. Lattice dynamics

3.4.1. Phonon dispersion

To confirm the dynamical stability of Ti_2PTe_2, we investigated its phonon dispersion and phonon density of states (PHDOS). The phonon dispersion, illustrated in Fig. 4, shows only positive phonon frequencies across the entire Brillouin zone, affirming the compound's dynamical stability. Additionally, the zero-phonon frequency observed at the Γ-point (zone center) further supports this stability. The phonon spectrum of hexagonal Ti_2PTe_2 consists of 15 branches, as its crystal structure contains five atoms per unit cell. These branches include three acoustic modes (represented by pink lines) and twelve optical modes (shown in green). The dispersion curves reveal that the acoustic modes, which occur at lower frequencies, are dominated by the oscillation of the heavier Te atoms. Meanwhile, the higher-frequency optical modes arise from the vibrations of lighter atoms, such as Ti and P. The PHDOS analysis highlights this distribution of vibrational modes, showing that the lower branches are driven by the motion of Te atoms, while the optical branches are primarily due to the vibrations of Ti and P atoms. The phonon density of states (DOS) in Fig. 4 reveals distinct, separated bands, allowing us to examine the vibrational contributions of Ti, P, and Te atoms. At lower frequencies, the acoustic modes are primarily influenced by the oscillations of the heavier Te atoms, with minimal contributions from Ti and P. This dominance of Te is particularly evident in the low-frequency optical modes, where the cyan peaks in the DOS plot highlight Te's significant role. In contrast, the higher-frequency optical modes are driven by the vibrations of lighter atoms, like Ti

Table 4
The calculated values of brittleness indicators (G/B and ν), hardness (H_{Chen} and H_{Miao} in GPa), machinability index (μ_M), and elastic anisotropy (A_1, A_2, and A_3) of Ti_2PTe_2.

Compound	ν	G/B	H_{Chen}	H_{Miao}	μ_M	A_1	A_2	A_3	k_c/k_a	Ref.
Ti_2PTe_2	0.25	0.578	4.32	4.61	1.73	0.68	0.68	1.00	6.75	This work

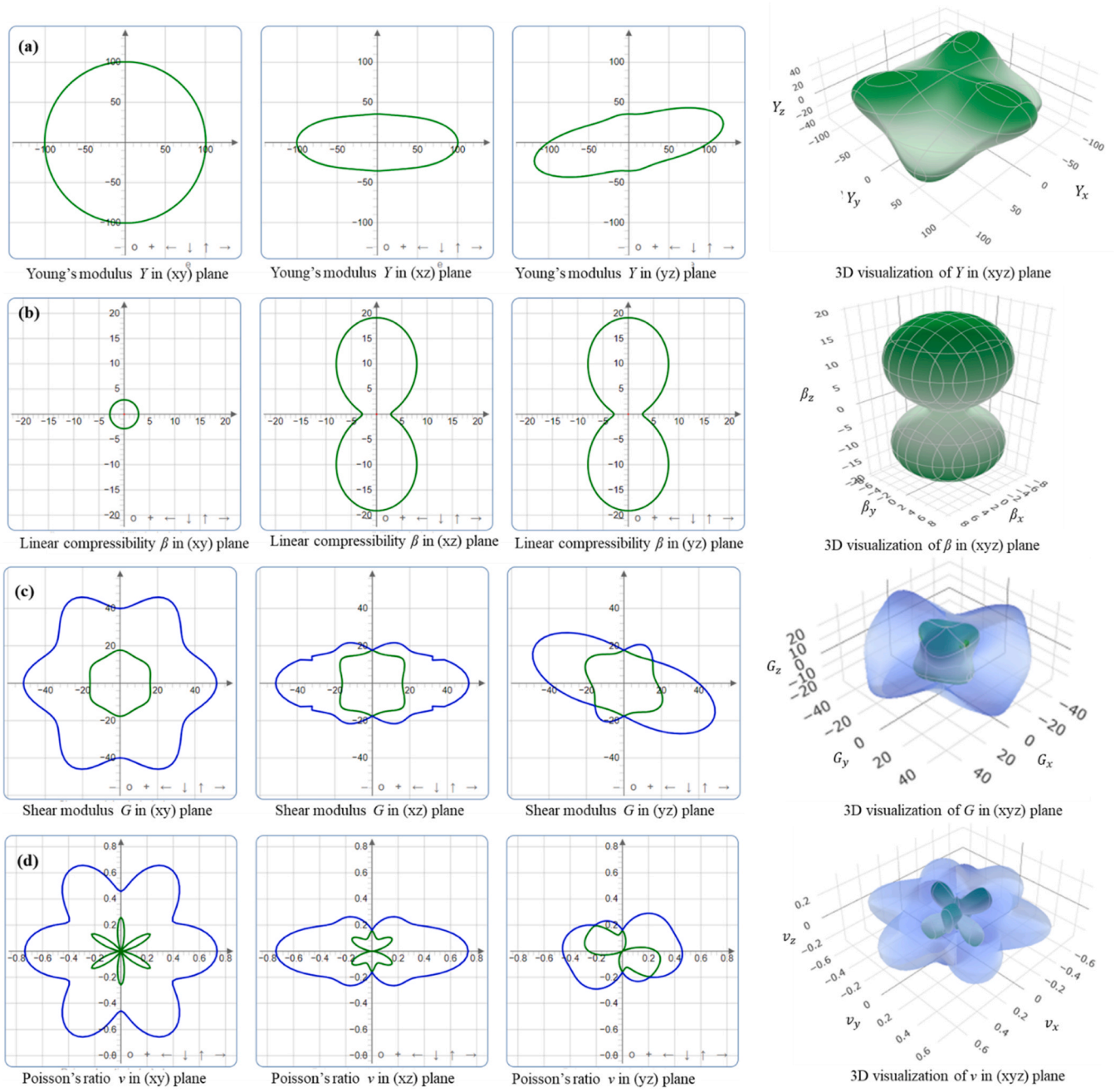

Fig. 3. Directional anisotropy (2D and 3D) of (a) Young's modulus (b) compressibility (c) shear modulus and (d) Poisson's ratio for Ti_2PTe_2.

Table 5
The calculated minimum, maximum limits, and anisotropy coefficients (Y in GPa), (β in TPa^{-1}), (G in GPa) and ν of Ti_2PTe_2.

Structure	Y			β			G			ν		
	Y_{min}	Y_{max}	A_Y	β_{min}	β_{max}	A_β	G_{min}	G_{max}	A_G	ν_{min}	ν_{max}	A_ν
Ti_2PTe_2	35.4	120.4	3.4	2.8	19.1	6.7	16.0	51.5	3.2	−0.01	0.73	∞

Table 6
Calculated Mulliken bond overlap population P^μ with bond number N^μ, bond length (d^μ in Å), metallic population $P^{\mu'}$, volume of μ-type bond (v_b^μ in $Å^3$), bond hardness (H_v^μ in GPa) and Vickers hardness (H_v in GPa) of Ti_2PTe_2.

Compound	Bond	N^μ	P^μ	d^μ	$P^{\mu'}$	v_b^μ	H_v^μ	H_v	Ref.
Ti_2PTe_2	P-Ti	6	0.88	2.48	0.006	23.64	3.32	2.96	This work
	Te-Ti	6	−0.37	2.79	0.006	33.66	2.64		

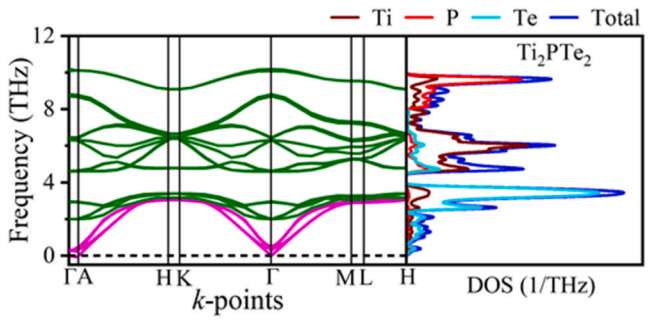

Fig. 4. The phonon dispersion curve for Ti_2PTe_2 chalcogenide.

and P.

In solids, heat is mainly carried by phonons, especially by acoustic phonons (low-frequency vibrations) because they propagate through the lattice, carrying energy over longer distances. Optical phonons, however, have shorter wavelengths and tend to be more localized. Due to their high energy and limited ability to propagate through the lattice, they contribute little to heat transport compared to acoustic phonons. The key interaction between these two types of phonons has a profound impact on thermal conductivity. When acoustic phonons, responsible for efficient heat conduction, encounter optical phonons, they scatter. This scattering disrupts the flow of heat, as acoustic phonons lose their momentum and ability to transport energy effectively. As a result, the material's overall thermal conductivity is significantly reduced. Furthermore, the optical modes are highly dispersive (refer to Fig. 4), contributing negligibly to heat conduction, as their interactions promote phonon scattering. The greatest contribution to the acoustic branch is attributed to Te atoms, whose heavier mass slows down phonon propagation and reduces thermal conductivity further. This phonon behavior, characterized by the interplay between optical and acoustic modes, emphasizes the role of Te in minimizing thermal conductivity, positioning Ti_2PTe_2 as a promising candidate for applications requiring effective thermal insulation. The behavior observed in this material is analogous to M_2C carbides (M = Tc, Ru, Rh, Pd, Re, Os, Ir, Pt), where similar phonon interactions lead to decreased thermal conductivity[86].

3.4.2. Debye temperature

The Debye temperature (Θ_D) is a key parameter for understanding the thermal, mechanical, and vibrational properties of crystalline solids. It represents the temperature at which a crystal's highest normal mode of vibration occurs, and influences critical properties such as thermal conductivity, specific heat, and bonding strength. Materials with higher Θ_D typically display lower atomic masses and exhibit reduced melting points. As shown in Table 7, the Debye temperature of Ti_2PTe_2, calculated using the Anderson method [39], is 266.0 K, indicating a relatively soft material with limited thermal conductivity. This value falls within the general range of 200–400 K reported for most crystals [87], aligning with expectations for Ti_2PTe_2. Moreover, Θ_D is often correlated with hardness, with higher values implying stronger bonding and greater resistance to deformation. While no prior data exists for Ti_2PTe_2 in the literature, these results provide essential insights into its physical characteristics and could serve as valuable benchmarks for future studies on similar compounds. The Debye temperature of Ti_2PTe_2 (Θ_D = 26 K) is much lower compared to other MAB phases, such as Zr_2InB_2 (Θ_D = 516 K), Zr_2TlB_2 (Θ_D = 433 K), Hf_2SnB_2 (Θ_D = 447K), Ti_2InB_2 (Θ_D = 633 K), and Hf_2InB_2 (Θ_D = 431 K)[80,81]. This implies that the bond strength in Ti_2PTe_2 is weaker, leading to lower phonon propagation efficiency and consequently lower lattice thermal conductivity. The low Θ_D value for Ti_2PTe_2 suggests that its ability to conduct heat through lattice vibrations is significantly reduced compared to other materials with higher Debye temperatures, which could be advantageous for applications requiring thermal insulation.

3.4.3. Melting temperature

The melting temperature (T_m) is a crucial indicator of a material's thermal stability and purity, marking the transition from solid to liquid. The melting temperature (T_m) of Ti_2PTe_2, calculated to be approximately 815 K (with an uncertainty of ±300 K), is moderate rather than particularly high. This moderate melting point indicates that while Ti_2PTe_2 offers some thermal stability, it may not be suitable for extreme high-temperature environments but can still perform well in applications that require intermediate levels of thermal endurance. A higher T_m reflects stronger interatomic forces and greater chemical stability, key for materials used in thermally demanding environments. The moderate T_m suggests that the interatomic forces in Ti_2PTe_2 are strong enough to ensure stability under reasonably high temperatures, but not as robust as in materials with much higher melting points. This makes Ti_2PTe_2 suitable for applications that need balanced thermal and mechanical resilience but don't require extreme heat resistance. The correlation between melting temperature and mechanical properties, like Young's modulus, also supports the idea that Ti_2PTe_2 has a solid structural framework. This balance of moderate thermal stability and reliable mechanical strength makes Ti_2PTe_2 versatile for a variety of industrial uses, particularly in applications that don't demand ultra-high-temperature endurance.

3.4.4. Minimum thermal conductivity

The minimum thermal conductivity (k_{min}) is critical for materials used in high-temperature applications, such as thermoelectrics and thermal barrier coatings (TBCs). Clark's theory suggests that materials reach a minimum thermal conductivity at elevated temperatures, making them ideal candidates for TBCs [88]. This minimum represents the theoretical lower limit where phonons are entirely uncoupled, crucial for high-temperature performance. In our study, the calculated k_{min} for Ti_2PTe_2 is 0.49 W/m-K, significantly below the benchmark value of 1.25 W/m-K [89]. The low minimum thermal conductivity (0.49 W.m^{-1}.K^{-1}) predicted for Ti_2PTe_2 and proved in many compounds like $Cu_2S_{1/3}Se_{1/3}Te_{1/3}$ (0.49 W.m^{-1}.K^{-1})[90], W/Al_2O_3 (0.6 W.m^{-1}.K^{-1})[91], and UT_2Si_2 (T = Ru, Rh, and Pd) (0.63–0.73 W.m^{-1}.K^{-1})[92], demonstrates its potential as an effective thermal insulator. According to Clarke's model[44], the minimum thermal conductivity is strongly influenced by the mean atomic weight (M) and the number of atoms per molecule (n), expressed as M/n in Eq. (20). Ti_2PTe_2's relatively high mean atomic weight of 76.38 amu/atom significantly contributes to its low thermal conductivity. This heavy atomic mass, combined with moderate Θ_D, results in slower heat transfer, making Ti_2PTe_2 an effective thermal insulator and a promising material for thermal barrier coatings (TBCs).

3.4.5. Lattice thermal conductivity

Lattice thermal conductivity (κ_{ph}) is a key property of solids, especially for materials used in high-temperature environments. It arises primarily from phonon contributions across all frequencies. For Ti_2PTe_2, the room-temperature lattice thermal conductivity is 3.03 $WK^{-1}m^{-1}$, as

Table 7
The calculated density (ρ in g/cm^3), velocities (v_t, v_l, v_a in ms^{-1}), Debye temperature (Θ_D in K), melting temperature (T_m in K), lattice and minimum thermal conductivities (κ_{ph}, k_{min} in W/m-K), thermal expansion coefficient ($\alpha \times 10^{-5}$ in K^{-1}), and heat capacity per unit volume ($\rho C_P \times 10^5$ in J/m^3.K).

Compound	ρ	V_t	V_l	V_a	Θ_D	T_m	k_{ph}	k_{min}	α	ρC_P	Ref.
Ti_2PTe_2	5.53	2229	6755	2536	266	815	3.17	0.49	5.82	1.43	This work

listed in Table 7, with its temperature dependence shown in Fig. 5. The Debye temperature of 266 K indicates that all vibrational modes are activated above this temperature, making phonon contributions dominant. From 100–800 K, the lattice conductivity gradually decreases as temperature increases, with electronic contributions being negligible. Comparing Ti_2PTe_2 with other materials like Ba_2ZrS_4, which has a κ_{ph} value of 3.43 $WK^{-1}m^{-1}$ and Ba_2HfS_4 with κ_{ph} of 3.12 $WK^{-1}m^{-1}$, it is clear that the thermal conductivities and Debye temperatures of these materials are in close agreement[93]. For example, Ba_2ZrS_4 has a Debye temperature of 285.8 K, and Ba_2HfS_4 has 268.7 K[93], both similar to the Debye temperature of Ti_2PTe_2 at 266 K. These closely values suggest that all these materials share a common phonon-driven mechanism for heat transport. Additionally, the minimum thermal conductivity (k_{min}) values for Ba_2ZrS_4 and Ba_2HfS_4 (0.45 $WK^{-1}m^{-1}$ and 0.42 $WK^{-1}m^{-1}$, respectively) [93] also align with Ti_2PTe_2 's behavior, where thermal conductivity reaches a minimum at high temperatures due to increased anharmonic scattering. The correlation between lattice thermal conductivity and Debye temperature highlights that, for materials like Ti_2PTe_2, phonon modes play the dominant role in heat transport, particularly above the Debye temperature. Every vibrational mode becomes active at this threshold, meaning that thermal management in such materials is predominantly governed by how these phonons behave across different temperatures.

3.4.6. Thermal expansion coefficient and heat capacity

The thermal expansion coefficient [67] ($\alpha = (1.6 \times 10^{-3})/G$)) plays a vital role in understanding how materials behave under varying thermal conditions, influencing properties such as specific heat, thermal conductivity, band gap energy, and electron effective mass. For Ti_2PTe_2, the thermal expansion coefficient, presented in Table 7, helps assess its suitability for various high-temperature applications.

Nahar *et al.* reported α values for $SnTaS_2$ (4.86×10^{-5} K^{-1}) and TaX (X = P, As) with α values of 1.42×10^{-5} K^{-1} and 1.74×10^{-5} K^{-1}, respectively, both used as TBC materials[67,94]. The calculated thermal expansion coefficient for Ti_2PTe_2 shows good agreement with these materials, indicating that Ti_2PTe_2 possesses thermal properties comparable to known TBC materials, enhancing its potential for similar applications. Heat capacity, another essential material property, is closely linked to thermodynamic behavior and affects a solid's mechanical, electrical, and optical characteristics. The heat capacity per unit volume, ρC_P, is expressed as $3k_B/\Omega$, where Ω is the atomic volume [67]. Higher heat capacity typically results in improved thermal conductivity and reduced thermal diffusivity. For Ti_2PTe_2, the calculated value of ρC_P further underscores its thermal performance.

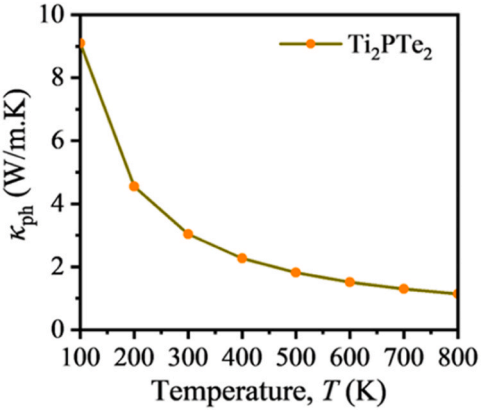

Fig. 5. The estimated lattice thermal conductivity of Ti_2PTe_2 as a function of temperature.

3.5. Electronic behavior

The electronic properties of Ti_2PTe_2, such as energy band dispersions and density of states (DOS), are crucial for understanding its optical and charge transport behavior. Using the GGA-PBE approximation, the band structures of Ti_2PTe_2 were calculated over an energy range of −4.0–4.0 eV, with the Fermi level (E_F) marked as a dotted line at 0 eV, as illustrated in Fig. 6**(a)**. This Kohn-Sham electronic band structure was obtained by plotting eigen energies (E) as a function of wavevector (k) within the first Brillouin zone (BZ). The BZ paths explored in these DFT computations connect high-symmetry points: Γ (0, 0, 0), A (0, 0, 0.5), H (-0.333, 0.667, 0.5), K (-0.333, 0.667, 0), Γ (0, 0, 0), M (0, 0.5, 0), and L (0, 0.5, 0.5). The electronic band structure of Ti_2PTe_2 reveals striking anisotropic properties, with several bands crossing the Fermi level along the Γ-M and L-H directions, confirming its metallic nature. In contrast, no band crossings are observed along the Γ-A, H-K, and M-L directions, highlighting significant directional differences in transport properties. This anisotropy is driven by strong hybridization between Ti-3d and Te-5p orbitals, with less contributions from P-3p states. In the band structure, energy dispersion refers to how the energy of electrons changes with their momentum (wavevector). High energy dispersion allows electrons or holes to gain energy easily and enhances conductivity, while low energy dispersion means less energy change with momentum, leading to reduced carrier mobility. For Ti_2PTe_2, the band structure reveals direction-dependent electrical conductivity due to variations in energy dispersion along different crystallographic paths. Specifically, the band paths along the *c*-direction (Γ-A, H-K, and M-L) exhibit a lower degree of energy dispersion compared to the paths in the *ab*-plane (A-H, K-Γ, Γ-M, and L-H). This lower dispersion along the *c*-axis leads to a higher effective mass for charge carriers moving in that direction, which results in lower electrical conductivity along the *c*-axis compared to the *ab*-plane. Thus, the anisotropic electrical conductivity of Ti_2PTe_2 is characterized by much lower conductivity along the *c*-axis than in the basal planes (*ab*-plane). This anisotropy is a direct consequence of the crystal's electronic band structure, making it important to consider for applications that rely on directional electrical properties. Similar anisotropic transport has been observed in different nanolaminated structures [95–97], like Ti_2AlC, where resistivity along the *c*-axis is significantly higher than in polycrystalline bulk [98]. This significant difference in carrier mobility underscores the highly anisotropic nature of Ti_2PTe_2, where transport properties are strongly direction-dependent, offering unique potential for tailored electronic applications.

To explore the electronic properties of the Ti_2PTe_2 chalcogenide phase, we performed calculations of the total and partial density of states (DOS), as shown in Fig. 6**(b)**. The DOS analysis reveals that Ti_2PTe_2 exhibits metallic behavior, evidenced by the notable DOS value of approximately 7.26 states/eV at the Fermi level (E_F). A higher DOS at E_F is often linked to improved conductivity, as it increases the number of available electronic states for transitions under an applied electric field. Focusing on the Brillouin zone's Γ point, we observe that the valence

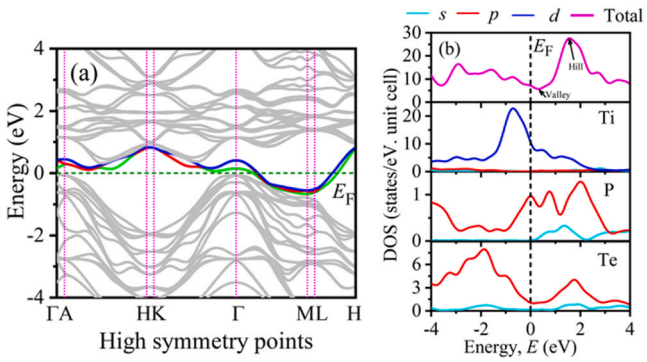

Fig. 6. Band structure of Ti_2PTe_2 with partial and total density of states.

band near the Fermi level along the Γ direction is steeper than in other directions. This steepness suggests that holes have a smaller effective mass along this path, which is confirmed by the Fermi velocity [97] ($v_F = \sqrt{E_F/m^*}$) at E_F. Here, v_F represents the velocity of charge carriers, and m^* is their effective mass. A steeper band curvature leads to lower effective mass, enhancing both the Fermi velocity and the material's conductive properties. As a result, the material exhibits greater efficiency in charge and heat transport, making it an excellent candidate for advanced electronic applications.

Metallicity (f_m) offers a compelling insight into a material's electronic properties, indicating the proportion of thermally excited electrons (n_m) compared to the total valence electrons (n_e). This ratio is given by [97,99]

$$f_m = \frac{n_m}{n_e} = \frac{k_B T \times N(E_F)}{n_e} = \frac{0.026 \times N(E_F)}{n_e} \tag{29}$$

At room temperature (around 300 K), 0.026 eV represents the thermal energy. The calculated f_m value of 2.7×10^{-3} shows that only about 0.27 % of the total valence electrons in Ti_2PTe_2 are thermally excited. This small f_m highlights the presence of a high density of states (DOS) at the Fermi level, a key trait of metallic behavior. Even though the material shows metallic characteristics, only a tiny fraction of electrons are thermally excited at room temperature. A similar trend is observed in M_2GaC (M = Zr, Hf) structures [97].

A key feature of Ti_2PTe_2 is the presence of a valley or pseudogap in the total density of states (TDOS) near the Fermi level, which contributes to the material's electrical stability [100,101]. Pseudogap, located between bonding and antibonding states, play a vital role in distinguishing these states. The pseudogap energy (E_P) lies to the right from the Fermi level, which indicates that the electrons above E_P become delocalized. This delocalization signifies the transition to metallic behavior, enhancing the material's conductive properties. From the analysis of Fig. 6**(b)**, it becomes clear that the valence band of Ti_2PTe_2 is predominantly shaped by the contributions from Ti-3d and Te-5p orbitals, with a less contribution from the P-3p orbital. Meanwhile, the transport properties are also largely influenced by the Ti-3d and Te-5p orbitals.

To further understand the bonding characteristics of Ti_2PTe_2 chalcogenides, Fig. 7 showcases the electron density distribution map along the (111) crystallographic plane. This map reveals the bonding nature between atoms, with color scales indicating charge intensity: blue for high electron density and red for low. Covalent bonds are identified by concentrated charges between atoms, while ionic bonds are suggested by a balance of positive and negative charges at atomic sites. Fig. 7 reveals a strong accumulation of charges around the Ti atoms, indicating significant electron density and suggesting robust covalent bonding between Ti and both Te or P atoms in Ti_2PTe_2. This is due to the strong hybridization between Ti-3d states and Te/P-5p/3p states. The lack of overlap in electron distributions between P and Te atoms points to an ionic nature in the P-Te bond. Additionally, the high charge concentration around Ti atoms suggests metallic bonding, contributing to the material's conductivity. Thus, Ti_2PTe_2 exhibits a fascinating combination of covalent, ionic, and metallic bonding.

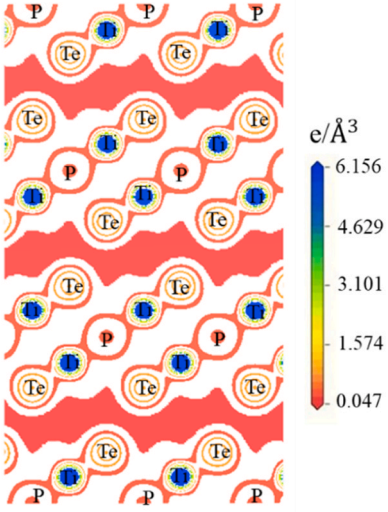

Fig. 7. Charge density maps for Ti_2PTe_2 along the (111) plane, highlighting electron distribution.

3.6. Optical properties

The optical properties of the metallic chalcogenide Ti_2PTe_2 have attracted great interest due to their promising applications in various technologies. This section emphasizes key optical features, including the real and imaginary parts of the dielectric function, absorption, optical conductivity, reflectivity, refractive index, and loss function, as illustrated in Fig. 8**(a-h)**. These properties, calculated across a photon energy range from 0 to 25 eV, reveal unique insights into the material's behavior. Polarization vectors along the [100] and [001] directions were examined, shedding light on the optical and electronic anisotropy. Both intra-band and inter-band transitions contribute to the dielectric functions of this metallic system, necessitating an empirical Drude model for accurate analysis [102,103]. In our study, we utilized a Drude damping factor of 0.05 eV and a plasma frequency of 6 eV for Ti_2PTe_2, offering further understanding of its optical characteristics and behavior under different electric field polarizations.

The real part of the dielectric function, $\varepsilon_1(\omega)$, along the [100] and [001] directions for Ti_2PTe_2 is shown in Fig. 8**(a)**, reflecting the material's polarizability. Notably, Ti_2PTe_2 exhibits prominent peaks in the low energy region, suggesting a low charge recombination rate, which enhances its potential in solar applications. In solar cells, low recombination rates are essential because they enhance the likelihood that generated charge carriers will be collected at the electrodes rather than recombining and dissipating energy. The optical reflectivity and absorption coefficient are strongly influenced by this real component. In the low energy range, $\varepsilon_1(\omega)$ crosses zero from negative values, confirming the metallic nature of Ti_2PTe_2. The large negative values further underscore its Drude-like behavior, characteristic of metals. Across the energy spectrum, both polarization directions display similar features, except within the 1.46–2.59 eV range. A subtle difference in the intensity of a peak at 1.83 eV in $\varepsilon_1(\omega)$ indicates slight anisotropy in the optical properties at low photon energies.

The imaginary part of the dielectric function, $\varepsilon_2(\omega)$, is another key factor in determining a crystal's optical properties, reflecting inter-band transitions between the valence and conduction bands. Fig. 8**(b)** illustrates $\varepsilon_2(\omega)$ for two photon polarizations, where it approaches zero from above, reaffirming again the metallic nature of Ti_2PTe_2. The first peaks observed at 2.08 eV arise from orbital electron transitions, specifically between Ti-3d and Te-5p or P-3s orbitals, from the highest valence to the lowest conduction bands. Intra-band transitions cause low-energy peaks, while higher-energy peaks stem from inter-band transitions. Beyond 17 eV, both $\varepsilon_1(\omega)$ and $\varepsilon_2(\omega)$ show similar behavior, further highlighting the material's complex optical characteristics and its potential for advanced technological applications.

The refractive index $n(\omega)$ plays a crucial role in designing advanced electronic devices. For Ti_2PTe_2, the static refractive index $n(0)$ is remarkably high (~168) in both polarization orientations, making it suitable for enhancing display quality in devices like LCDs and quantum dot TVs. In the visible region, the refractive index sharply rises due to intra-band electron transitions, reaching a peak of 3.36 at 1.96 eV (see Fig. 8**(c)**). Beyond this point, $n(\omega)$ decreases continuously and exhibits slight anisotropy up to 25 eV, highlighting its versatile optical properties.

The extinction coefficient $k(\omega)$ measures absorption loss as electromagnetic radiation travels through a medium. Fig. 8**(d)** presents the

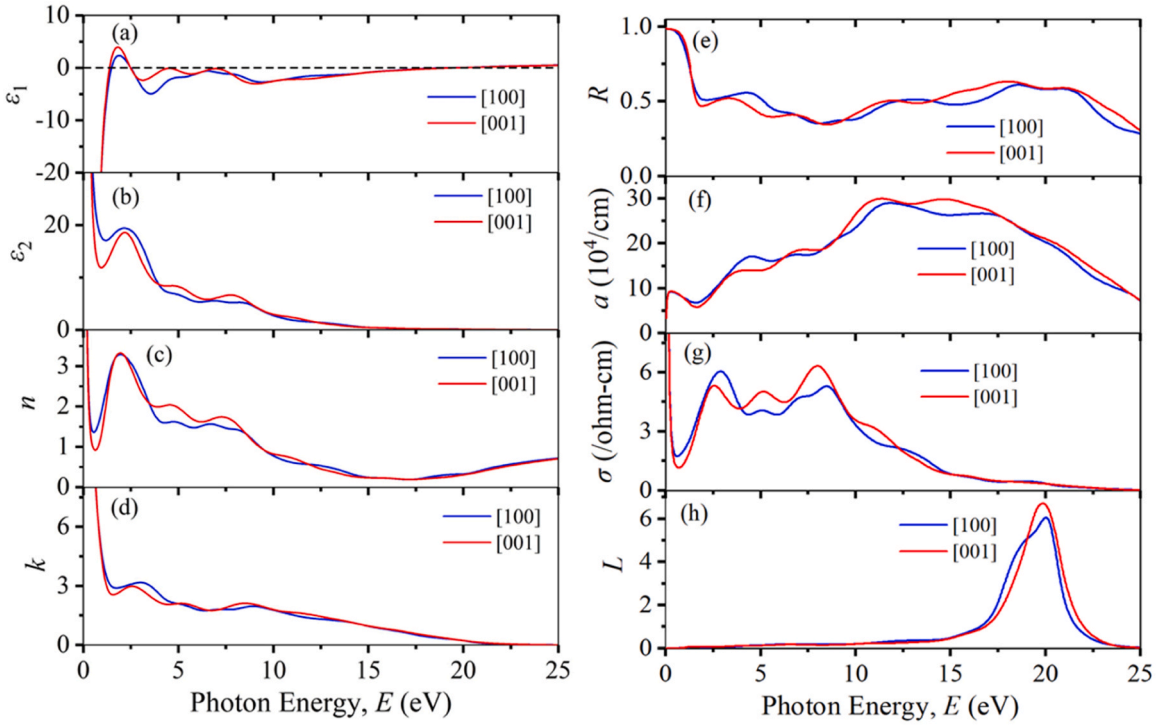

Fig. 8. The energy dependent (a) real part of dielectric function, (b) imaginary part of dielectric function, (c) refractive index, (d) extinction coefficient, (e) reflectivity, (f) absorption coefficient, (g) optical conductivity, and (h) loss function of Ti_2PTe_2 along [100] and [001] polarization directions.

extinction coefficient of Ti_2PTe_2 for two polarizations, revealing slight anisotropy between 1.12 and 13.36 eV. The trend in $k(\omega)$ closely parallels that of $\varepsilon_2(\omega)$, highlighting its role in measuring the absorption of incident radiation.

Reflectivity $R(\omega)$ measures the fraction of energy from a wave reflected off a material's surface. Fig. 8**(e)** presents the optical reflectivity of Ti_2PTe_2, where both polarizations exhibit similar reflectivity spectra, starting at approximately 0.99. The reflectivity increases significantly in both the moderate infrared and ultraviolet regions. In the visible light range (~1.67–3.10 eV), reflectivity ranges from 51 % to 55 % along the [100] direction and 47–50 % along the [001] direction. This prevents excessive heat buildup in solar cells, which can degrade efficiency. By reflecting unwanted infrared and ultraviolet radiation, Ti_2PTe_2 helps maintain lower operating temperatures, allowing solar cells to perform optimally, especially in hot climates. It has been predicted that materials like Hf_2AB_2 (A = In, Sn), M_3PbC_2 (M = Zr, Hf), Ti_3SiC_2 and Ti_4AlN_3 with reflectivity above 44 % can effectively reduce solar heating[102,104,105]. In this context, Ti_2PTe_2 meets this criterion with its consistent reflectivity exceeding 44 %, making it a strong candidate for use in solar heat-reducing coatings. Additionally, the material is expected to appear metallic gray due to its nearly uniform reflectivity in the visible spectrum. The reflectivity spectra also reveal slight anisotropy across the photon energy range.

The absorption coefficient (α) quantifies how much electromagnetic energy is absorbed by a material as light propagates through it. For Ti_2PTe_2, the absorption spectra, shown in Fig. 8**(f)**, begin at zero photon energy, reflecting its metallic nature. When Ti_2PTe_2 absorbs photons, it generates electron-hole pairs. Due to its metallic character, the material can efficiently transport these charge carriers, ensuring they reach the electrodes with minimal recombination losses. The ability to generate and collect these carriers effectively leads to improved performance in solar cells. As photon energy increases, the absorption rises, reaching its peak in the ultraviolet (UV) region for bot h [100] and [001] polarizations. This highlights Ti_2PTe_2 as a highly efficient material for absorbing UV light. The absorption reaches a maximum of 30×10^4 cm^{-1} at 9.03 eV in the [001] direction and 29×10^4 cm^{-1} at 9.24 eV in the [100] direction. After the peak, the absorption coefficient decreases as photon energy continues to rise. The stronger absorption in the UV region suggests potential applications in UV detectors, anti-reflective coatings, and materials for protecting sensitive systems from photo-disintegration or photo-oxidation. Additionally, the absorption spectra exhibit slight anisotropy across nearly the entire photon energy range, making Ti_2PTe_2 a versatile material for advanced optical technologies.

Optical conductivity $\sigma(\omega)$ describes how a material responds to an alternating electric field at optical frequencies. It is a measure of how effectively the material conducts electric currents when exposed to light or other forms of electromagnetic radiation, typically in the visible, infrared, or ultraviolet range. When an alternating electric field (such as light) interacts with a material, it excites the charge carriers (primarily electrons). These excited electrons oscillate in response to the alternating field. Optical conductivity quantifies how easily these oscillating electrons can move through the material, which is analogous to how the material conducts electricity under a direct electric field (DC conductivity) but at much higher frequencies. In the case of Ti_2PTe_2, the optical conductivity graph in Fig. 8**(g)** shows significant peaks at photon energies of 2.89 eV and 7.98 eV for the [100] and [001] directions, respectively. These peaks indicate that Ti_2PTe_2 exhibits high electrical conductivity when photons at these energy levels interact with the material. Essentially, light at these energies excites the electrons in Ti_2PTe_2, enabling them to move more freely and generate strong electrical currents. This high optical conductivity signifies that the material can effectively conduct electricity when interacting with light of specific energies. Additionally, Ti_2PTe_2 displays anisotropy, meaning that its optical conductivity varies based on the direction of the applied electric field. The differing conductivity between the [100] and [001] crystallographic directions indicates that the material responds differently to light depending on the direction of the incoming field. This directional behavior is particularly useful in applications like solar cells, where the material's orientation can be optimized to maximize electrical performance and efficiency.

The energy loss function $L(\omega)$ reflects the energy lost by fast electrons as they traverse through a material. As depicted in Fig. 8**(h)**, Ti_2PTe_2

shows no peaks between 0–16 eV, attributed to the high values of $\varepsilon_2(\omega)$. However, significant peaks appear between 16–23 eV, indicating plasma oscillations. These peaks correspond to the material's bulk plasma frequency, which occurs when $\varepsilon_1(\omega)$ reaches zero and $\varepsilon_2(\omega)$ approaches minimal values. At this point, the material transitions from metallic to dielectric behavior. For Ti_2PTe_2, bulk plasma frequencies are observed at 20.1 and 19.8 eV along the [100] and [001] directions, respectively. Beyond these frequencies, the material exhibits transparency, evidenced by sharp declines in reflectivity and absorption.

3.7. Thermal properties

We investigated the thermodynamic properties of Ti_2PTe_2 using the Gibbs2 program within the quasi-harmonic approximation[106], calculated at zero pressure in the 0–800 K temperature range. This range ensures that the quasi-harmonic model remains valid, with the results shown in Fig. 9**(a-f)**. Key properties include internal energy (U), Helmholtz free energy (H), entropy (S), heat capacities (C_V and C_P), thermal expansion coefficient (α_v), and Debye temperature (θ_D), all derived using the wien2k code.

The calculated internal energy (U) and Helmholtz free energy (H) of Ti_2PTe_2, as shown in Fig. 9**(a)**, exhibit typical temperature-dependent behavior for solids. At temperatures below 100 K, both U and H are close to zero. As the temperature rises above 100 K, the free energy (H) gradually decreases—a common trend in solids as they move toward states of lower energy. In contrast, the internal energy (U) increases steadily with temperature, reflecting the typical rise in thermal energy within the material.

As shown in Fig. 9**(b)**, the entropy (S) increases with temperature due to the heightened thermal agitation, causing greater disorder within the system. This rise in entropy is expected as thermal disturbances create more random motion among atoms. As the temperature continues to increase, this disorder grows, pushing the system toward higher entropy states, in line with natural processes. Ultimately, the interplay of decreasing free energy and increasing entropy mirrors the inherent drive of systems to find equilibrium at elevated temperatures.

Figs. 9**(c)** and 9**(d)** highlight the temperature dependence of the specific heats, C_V and C_P, for Ti_2PTe_2 between 0 and 800 K. At low temperatures, both C_V and C_P rise sharply due to the exponential increase in phonon modes, as described by the Debye T^3-law. This rapid increase reflects the material's sensitivity to thermal excitation at lower temperatures. As temperature continues to rise, phonon thermal softening occurs, gradually slowing the rate of increase in specific heat. In higher temperature regimes, C_V and C_P approach the classical Dulong-Petit limit ($3nN_Ak_B$), a well-established behavior for most solids. This limit suggests that the anharmonic effects influencing specific heat become less significant as temperature rises. The specific heat's convergence toward the Dulong-Petit limit indicates that, at higher temperatures, the phonon modes in Ti_2PTe_2 behave in a manner consistent with classical predictions, with less deviation due to thermal vibrations. At temperatures below 300 K, C_V follows a T^3 relationship, typical for solids with low thermal excitation. However, above 300 K, the heat capacity behavior stabilizes, signifying a transition toward the Dulong-Petit limit as the number of excited phonons saturates. This behavior highlights the balance between anharmonicity at lower temperatures and classical predictions at higher temperatures, reflecting Ti_2PTe_2's sophisticated thermal response.

The thermal expansion coefficient (α_v) of Ti_2PTe_2, as shown in Fig. 9 **(e)**, reflects the material's response to temperature changes, primarily due to anharmonicity in the lattice dynamics. This anharmonicity causes atoms to vibrate more intensely as temperature rises, leading to an expansion of the material. The α_v increases rapidly at temperatures below 100 K, where the anharmonic effects are most pronounced. However, as temperature surpasses 200 K, the rate of increase slows down and eventually saturates. At 300 K, Ti_2PTe_2 exhibits a α_v value of 11.48×10^{-5} K^{-1}, which is relatively moderate. This lower α_v is influenced by the material's bulk modulus, where a stiffer structure (higher bulk modulus) usually correlates with lower thermal expansion. Ti_2PTe_2's moderate expansion properties suggest it has good thermal stability, making it ideal for applications where minimal thermal distortion is crucial.

The Debye temperature (θ_D) is an important parameter that reflects the vibrational properties of a material's atomic lattice. It is closely related to the maximum vibrational frequency (or phonon energy) that atoms in the material can experience. As seen in Fig. 9**(f)**, the Debye temperature for Ti_2PTe_2 decreases as the temperature rises. This trend occurs because increasing temperature provides more thermal energy to

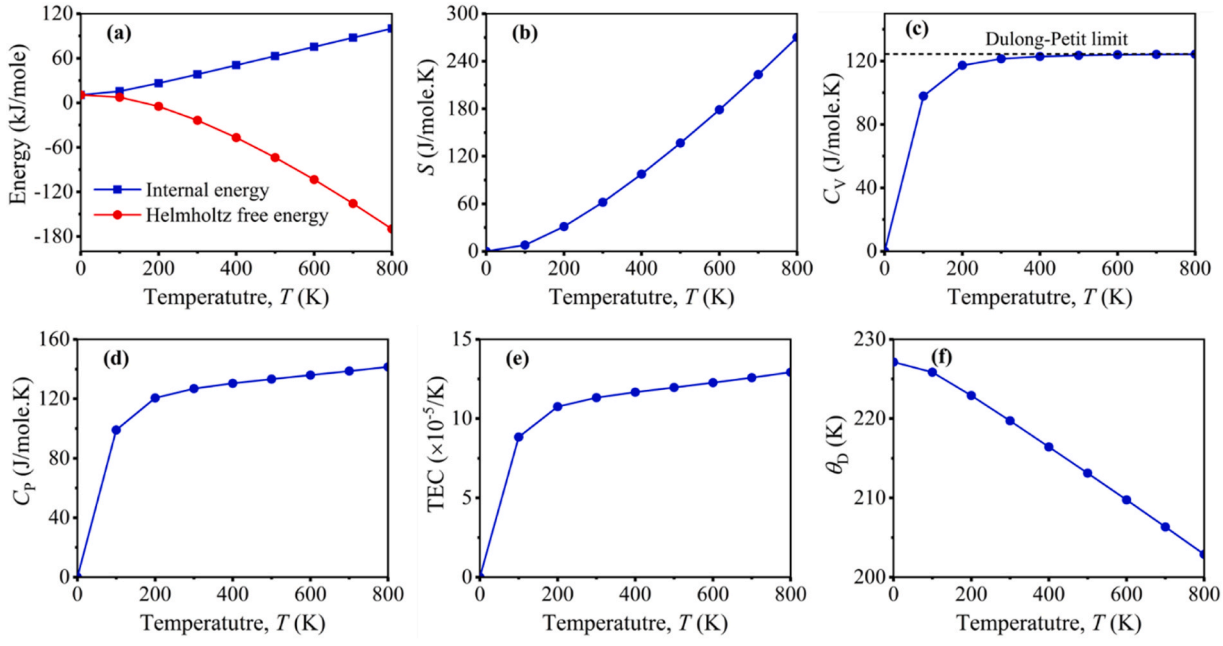

Fig. 9. The temperature-dependent thermodynamic characteristics of Ti_2PTe_2: (a) internal energy (U) and Helmholtz free energy (F), (b) entropy (S), (c) constant volume heat capacity (C_V), (d) constant pressure heat capacity (C_P), (e) thermal expansion coefficient (α_v), and (f) Debye temperature (θ_D).

the atomic lattice, leading to enhanced atomic vibrations. As temperature rises, these vibrations disrupt the material's interatomic bonds, effectively softening them. This softening lowers the vibrational frequencies of the phonons, which in turn reduces the Debye temperature. A similar trend has been observed in materials like Hf_2AB_2 (A = In, Sn) [81].

To the best of our knowledge, this work is the first to examine all thermal properties for Ti_2PTe_2 chalcogenide. We therefore anticipate that our results will be a useful direction for future research.

4. Conclusion

In this study, we explore the structural, mechanical, lattice dynamical, electronic, optical and thermal properties of Ti_2PTe_2 using first-principles calculations for the first time. Our findings reveal that Ti_2PTe_2's lattice parameters are in excellent agreement with experimental data. The stability of Ti_2PTe_2 has been confirmed across thermodynamic, mechanical, and dynamical aspects. The material's Vickers hardness, along with Chenn and Miao values, reveals its soft nature, while its Poisson's ratio and Pugh's ratio indicate brittleness. Ti_2PTe_2 demonstrates remarkable mechanical characteristics, with its stability more influenced by shear than compression ($B > G$), making it an excellent candidate for advanced engineering applications. The high Young's modulus (Y) further underscores its stiffness and effective thermal conductivity, making it ideal for heat management solutions. The fracture toughness of 0.30 MPa·$m^{1/2}$ is moderate when compared with other chalcogenide, and the brittleness index suggests a relatively brittle nature. Ti_2PTe_2 also demonstrates pronounced mechanical anisotropy, vividly depicted through 2D and 3D visualizations that reveal clear deviations from uniform shapes. It's thermal conductivity of 0.49 W/m-K, well below reference value 1.25 W/m-K, is ideal for TBCs. The Debye temperature of 266 K confirms dominant phonon contributions to its thermal behavior, reinforcing its potential for effective thermal insulation. The electronic band structure and density of states confirm Ti_2PTe_2's metallic behavior. This is primarily driven by Ti-3d and Te-5p orbitals. Notably, conductivity is higher along the c-axis than in the basal plane due to pronounced anisotropy. The steep valence band near the Fermi level in the Γ direction implies a lower effective mass and a higher Fermi velocity, thus optimizing the efficiency of charge and heat transport. The electronic charge density distribution reveals that Ti_2PTe_2 exhibits a combination of ionic, covalent, and metallic bonding. Its high static refractive index (~168) and impressive reflectivity (51 %-55 % along [100] and 47 %-50 % along [001]) make it suitable for advanced display technologies and solar heating reduction. Furthermore, Ti_2PTe_2's strong UV absorption highlights its potential for UV applications and anti-reflective coatings. The metallic nature of Ti_2PTe_2 is crucial for its potential in solar cell applications. Its high electrical conductivity, low charge recombination rates, effective light interaction, and strong absorption capabilities make it a promising candidate for enhancing solar energy conversion efficiency. Additionally, the thermal properties reveal that the specific heat follows the Debye T^3 power-law at low temperatures. At high temperatures ($T >$ 300 K), anharmonic effects are suppressed, and C_V approaches the Dulong-Petit limit. We believe that this study will inspire further exploration and development, driving innovation and expanding the use of these materials beyond traditional boundaries.

CRediT authorship contribution statement

M. H. Mia: Conceptualization; Investigation; Methodology; Writing manuscript-reviewing and editing; Validation; Supervision. **Mst. A. Khatun:** Methodology; Original draft preparation; Data curation; Software; Validation; Resources. **M. Rahman:** Formal analysis; Electronic properties analysis.

Declaration of Competing Interest

The authors declare that they have no known competing financial interests or personal relationships that could have appeared to influence the work reported in this paper.

Data availability

Relevant data from this study are available from the corresponding author upon a reasonable request.

References

[1] A. Zakery, Stephen Richard Elliott, Optical nonlinearities in chalcogenide glasses and their applications., 135, Springer Science & Business Media, 2007.

[2] Mehmet Ates, Ersen Yılmaz, Mehmet Kayra Tanaydın, Challenges, novel applications, and future prospects of chalcogenides and chalcogenide-based nanomaterials for photocatalysis. Chalcogenide-based nanomaterials as photocatalysts, Elsevier, 2021, pp. 307–337.

[3] Fuchs, Harald, and Thomas Schimmel. "Atomic sites of a bare surface modified with the tunneling microscope." (1991): 112-113.

[4] H. Fuchs, R. Laschinski, Th Schimmel, Atomic resolution of nanometer scale plastic surface deformations by scanning tunnelling microscopy, Europhys. Lett. 13 (4) (1990) 307.

[5] Fadiyah Makin, Binary and ternary metal chalcogenides for sustainable and inexpensive solar energy generation, The University of Manchester, United Kingdom, 2022.

[6] Abdolnasser Zakery, S.R. Elliott, Optical properties and applications of chalcogenide glasses: a review, J. Non-Cryst. Solids 330 (1-3) (2003) 1–12.

[7] Jayaraman Theerthagiri, K. Karuppasamy, Govindarajan Durai, Abu Ul. Hassan Sarwar Rana, Prabhakarn Arunachalam, Kirubanandam Sangeetha, Parasuraman Kuppusami, Hyun-Seok Kim, Recent advances in metal chalcogenides (MX; X= S, Se) nanostructures for electrochemical supercapacitor applications: a brief review, Nanomaterials 8 (4) (2018) 256.

[8] Wei Zhang, Rui Yu, Hai-Jun Zhang, Xi Dai, Zhong Fang, First-principles studies of the three-dimensional strong topological insulators Bi2Te3, Bi2Se3 and Sb2Te3, N. J. Phys. 12 (6) (2010) 065013.

[9] Z. Nabi, A. Kellou, S. Mecabih, A. Khalfi, N. Benosman, Opto-electronic properties of rutile SnO2 and orthorhombic SnS and SnSe compounds, Mater. Sci. Eng.: B 98 (2) (2003) 104–115.

[10] Lei Guo, Shengtao Zhang, Wenjiang Feng, Ge Hu, Wenpo Li, A first-principles study on the structural, elastic, electronic, optical, lattice dynamical, and thermodynamic properties of zinc-blende CdX (X= S, Se, and Te), J. Alloy. Compd. 579 (2013) 583–593.

[11] Sikander Azam, Muhammad Irfan, Zeesham Abbas, Malika Rani, Tahira Saleem, Ayesha Younus, Naseem Akhtar, Bushra Liaqat, Muhammad Shabbir, Abdullah G. Al-Sehemi, DFT study of the electronic and optical properties of ternary chalcogenides AlX2Te4, Mater. Res. Express 6 (11) (2019) 116314.

[12] Takeshi Nomura, Tsuyoshi Maeda, Takahiro Wada, Preparation of narrow band-gap Cu2Sn (S, Se) 3 and fabrication of film by non-vacuum process, Jpn. J. Appl. Phys. 52 (4S) (2013) 04CR08.

[13] Ying-Teng Zhai, Shiyou Chen, Ji-Hui Yang, Hong-Jun Xiang, Xin-Gao Gong, Aron Walsh, Joongoo Kang, Su-Huai Wei, Structural diversity and electronic properties of Cu 2 Sn X 3 (X= S, Se): A first-principles investigation, Phys. Rev. B—Condens. Matter Mater. Phys. 84 (7) (2011) 075213.

[14] Man-Ning Lu, Jeng-Yu Lin, Tzu-Chien Wei, Exploring the main function of reduced graphene oxide nano-flakes in a nickel cobalt sulfide counter electrode for dye-sensitized solar cell, J. Power Sources 332 (2016) 281–289.

[15] Xiaojia Zheng, Jiahao Guo, Yantao Shi, Fengqiang Xiong, Wen-Hua Zhang, Tingli Ma, Can Li, Low-cost and high-performance CoMoS 4 and NiMoS 4 counter electrodes for dye-sensitized solar cells, Chem. Commun. 49 (83) (2013) 9645–9647.

[16] Shan-Long Chen, Jie Tao, Hai-Bo Shu, Hai-Jun Tao, Yu-Xin Tang, Yi-Zhou Shen, Tao Wang, Lei Pan, Efficient electron transfer kuramite Cu3SnS4 nanosheet thin film towards platinum-free cathode in dye-sensitized solar cells, J. Power Sources 341 (2017) 60–67.

[17] Bingkun Chen, Shuai Chang, Deyao Li, Liangliang Chen, Yongtian Wang, Tao Chen, Bingsuo Zou, Haizheng Zhong, Andrey L. Rogach, Template synthesis of CuInS2 nanocrystals from In2S3 nanoplates and their application as counter electrodes in dye-sensitized solar cells, Chem. Mater. 27 (17) (2015) 5949–5956.

[18] Lei, Shuijin, Kaibin Tang, Yunxia Qi, Zhen Fang, and Huagui Zheng. "A Self-Sacrificing Template Route to Spinel MIIIn2S4 (MII= Mn, Zn, Cd, Fe, Co, Ni) and MIIn5S8 (MI= Cu, Ag) Porous Microspheres." (2006): 2406-2410.

[19] Horacio Falcón, Pedro Tartaj, Fernando Vaquero, Rufino M. Navarro, Jose Luis G. Fierro, Juan P. Bolletta, Juan M. de Paoli, Raul E. Carbonio, Maria Teresa Fernández-Díaz, Jose Antonio Alonso, Straightforward High-Pressure Synthesis and Characterization of Indium-Based Thiospinels: Photocatalytic Potential for Hydrogen Production, Eur. J. Inorg. Chem. 2016 (10) (2016) 1558–1565.

[20] Michel Armand, J.-M. Tarascon, Building better batteries, nature 451 (7179) (2008) 652–657.

[21] Bruce Dunn, Haresh Kamath, Jean-Marie Tarascon, Electrical energy storage for the grid: a battery of choices, Science 334 (6058) (2011) 928–935.
[22] Baoxin Ge, Biyi Chen, Longhua Li, Ternary transition metal chalcogenides Ti2PX2 (X= S, Se, Te) anodes for high performance metal-ion batteries: a DFT study, Appl. Surf. Sci. 550 (2021) 149177.
[23] J.P. Perdew, K. Burke, M. Ernzerhof, Generalized Gradient Approximation Made Simple, Phys. Rev. Lett. 77 (1996) 3865–3868, https://doi.org/10.1103/PhysRevLett.77.3865.
[24] Stewart J. Clark, Matthew D. Segall, Chris J. Pickard, Phil J. Hasnip, Matt I. J. Probert, Keith Refson, Mike C. Payne, First principles methods using CASTEP, Z. F. üR. Krist. -Cryst. Mater. 220 (5-6) (2005) 567–570.
[25] M.D. Segall, Philip J.D. Lindan, M.J. al Probert, Christopher James Pickard, Philip James Hasnip, S.J. Clark, M.C. Payne, First-principles simulation: ideas, illustrations and the CASTEP code, J. Phys.: Condens. Matter 14 (11) (2002) 2717.
[26] Hendrik J. Monkhorst, James D. Pack, Special points for Brillouin-zone integrations, Phys. Rev. B 13 (12) (1976) 5188.
[27] K. Akter, F. Parvin, M.A. Hadi, A.K.M.A. Islam, Insights into the predicted Hf2SN in comparison with the synthesized MAX phase Hf2SC: A comprehensive study, Comput. Condens. Matter 24 (2020) e00485.
[28] Amir Aliakbari, Peiman Amiri, Abdolmohammad Ghalambor Dezfuli, Stability and physical properties of yttrium-based new MAX phases Y2AX (A= Al, Si, Ga, and Ge; X= C and N): a first-principles prediction, Appl. Phys. A 129 (7) (2023) 476.
[29] F.élix Mouhat, François-Xavier Coudert, Necessary and sufficient elastic stability conditions in various crystal systems, Phys. Rev. B 90 (22) (2014) 224104.
[30] J.Peter Watt, Louis Peselnick, Clarification of the Hashin-Shtrikman bounds on the effective elastic moduli of polycrystals with hexagonal, trigonal, and tetragonal symmetries, J. Appl. Phys. 51 (3) (1980) 1525–1531.
[31] Richard Hill, The elastic behaviour of a crystalline aggregate, Proc. Phys. Soc. Sect. A 65 (5) (1952) 349.
[32] Ahmed Gueddouh, Bachir Bentria, I.K. Lefkaier, First-Principle Investigations of Structure, Elastic and Bond Hardness of FexB (X= 1, 2, 3) under Pressure, J. Magn. Magn. Mater. 406 (2016) 192–199.
[33] Xing-Qiu Chen, Haiyang Niu, Dianzhong Li, Yiyi Li, Modeling hardness of polycrystalline materials and bulk metallic glasses, Intermetallics 19 (9) (2011) 1275–1281.
[34] Naihua Miao, Baisheng Sa, Jian Zhou, Zhimei Sun, Theoretical investigation on the transition-metal borides with Ta3B4-type structure: A class of hard and refractory materials, Comput. Mater. Sci. 50 (4) (2011) 1559–1566.
[35] Huiyang Gou, Li Hou, Jingwu Zhang, Faming Gao, Pressure-induced incompressibility of ReC and effect of metallic bonding on its hardness, Appl. Phys. Lett. 92 (24) (2008).
[36] Haiyang Niu, Shiwei Niu, Artem R. Oganov, Simple and accurate model of fracture toughness of solids, J. Appl. Phys. 125 (6) (2019).
[37] Efim Mazhnik, Artem R. Oganov, A model of hardness and fracture toughness of solids, J. Appl. Phys. 126 (12) (2019).
[38] M.A. Hadi, Nikolaos Kelaidis, S.H. Naqib, Alexander Chroneos, A.K.M.A. Islam, Mechanical behaviors, lattice thermal conductivity and vibrational properties of a new MAX phase Lu2SnC, J. Phys. Chem. Solids 129 (2019) 162–171.
[39] D.H. Chung, W.R. Buessem, The Elastic Anisotropy of Crystals, J. Appl. Phys. 38 (1967) 2010.
[40] M.E. Fine, L.D. Brown, H.L. Marcus, Elastic constants versus melting temperature in metals, Scr. Metall. 18 (9) (1984) 951–956.
[41] Donald T. Morelli, Glen A. Slack, High lattice thermal conductivity solids. In High thermal conductivity materials, NY: Springer New York, New York, 2006, pp. 37–68.
[42] Vladimir Nikolaevich Belomestnykh, Elena Pavlovna Tesleva, Interrelation between anharmonicity and lateral strain in quasi-isotropic polycrystalline solids, Tech. Phys. 49 (8) (2004).
[43] Carl L. Julian, Theory of heat conduction in rare-gas crystals, Phys. Rev. 137 (1A) (1965) A128.
[44] David R. Clarke, Materials selection guidelines for low thermal conductivity thermal barrier coatings, Surf. Coat. Technol. 163 (2003) 67–74.
[45] Mark Fox, Optical properties of solids, 3, Oxford university press, 2010.
[46] Akihiro Kojima, Kenjiro Teshima, Yasuo Shirai, Tsutomu Miyasaka, Organometal halide perovskites as visible-light sensitizers for photovoltaic cells, J. Am. Chem. Soc. 131 (17) (2009) 6050–6051.
[47] Qi-Jun Liu, Ning-Chao Zhang, Fu-Sheng Liu, Hong-Yan Wang, Zheng-Tang Liu, BaTiO3: Energy, geometrical and electronic structure, relationship between optical constant and density from first-principles calculations, Opt. Mater. 35 (12) (2013) 2629–2637.
[48] Mingzhu Yang, Benkang Chang, Guanghui Hao, Jing Guo, Honggang Wang, Meishan Wang, Comparison of optical properties between Wurtzite and zinc-blende Ga0. 75Al0. 25N, Optik 125 (1) (2014) 424–427.
[49] Ayash O. Alrashdi, Anila Asif, Mohammed M. Fadhali, Abu Bakar, A. Afaq, Jehan Alqahtani, First principles calculations to investigate electronic, magnetic anisotropy energy and optical properties of MnCrP half-Heusler alloy, J. Mater. Res. Technol. 20 (2022) 4220–4230.
[50] Charles George Broyden, The convergence of a class of double-rank minimization algorithms 1. general considerations, IMA J. Appl. Math. 6 (1) (1970) 76–90.
[51] Charles G. Broyden, The convergence of a class of double-rank minimization algorithms: 2. The new algorithm, IMA J. Appl. Math. 6 (3) (1970) 222–231.
[52] Georg K.H. Madsen, David J. Singh, BoltzTraP. A code for calculating band-structure dependent quantities, Comput. Phys. Commun. 175 (1) (2006) 67–71.
[53] Jie Liu, Man Qiao, Xiaorong Zhu, Yu Jing, Yafei Li, Ti 2 PTe 2 monolayer: a promising two-dimensional anode material for sodium-ion batteries, RSC Adv. 9 (27) (2019) 15536–15541.
[54] Frauke Philipp, Peer Schmidt, Michael Ruck, Walter Schnelle, Anna Isaeva, The layered metal Ti2PTe2, J. Solid State Chem. 181 (10) (2008) 2859–2863.
[55] M. Guenfoud, M. Hamouda, I. Arbaoui, First-principles studies of the structural, elastic, vibrational, and thermodynamic properties of nonlinear chalcogenide LiGaTe 2 under pressure, Chalcogenide Lett. 18 (9) (2021).
[56] Sahib Hasan, Puja Adhikari, Khagendra Baral, Wai-Yim Ching, Conspicuous interatomic bonding in chalcogenide crystals and implications on electronic, optical, and elastic properties, AIP Adv. 10 (7) (2020).
[57] J. Worgull, E. Petti, J. Trivisonno, Behavior of the elastic properties near an intermediate phase transition in Ni 2 MnGa, Phys. Rev. B 54 (22) (1996) 15695.
[58] J. Pokluda, M. Černý, Mojmír Šob, Y. Umeno, Ab initio calculations of mechanical properties: Methods and applications, Prog. Mater. Sci. 73 (2015) 127–158.
[59] Leonard Kleinman, Deformation potentials in silicon. I. Uniaxial strain, Phys. Rev. 128 (6) (1962) 2614.
[60] Gao Qing-He, Xu Zhi-Jun, Tang Ling, Zuo Xianjun, Jia Guozhu, Du An, Linghu Rong-Feng, Guo Yun-Dong, Yang Ze-Jin, Evidence of the stability of Mo2TiAlC2 from first principles calculations and its thermodynamical and optical properties, Comput. Mater. Sci. 118 (2016) 77–86.
[61] Y.W. Bao, X.H. Wang, H.B. Zhang, Y.C. Zhou, Thermal shock behavior of Ti3AlC2 from between 200° C and 1300° C, J. Eur. Ceram. Soc. 25 (14) (2005) 3367–3374.
[62] Yanchun Zhou, Huimin Xiang, Fuzhi Dai, Zhihai Feng, "M2YSi (M= Rh, Ir): Theoretically predicted damage-tolerant MAX phase-like layered silicides.", J. Am. Ceram. Soc. 101 (1) (2018) 365–375.
[63] Yanchun Zhou, Huimin Xiang, Haiming Zhang, Fu-Zhi Dai, Theoretical prediction on the stability, electronic structure, room and elevated temperature properties of a new MAB phase Mo2AlB2, J. Mater. Sci. Technol. 35 (12) (2019) 2926–2934.
[64] Md. Nasir Uddin, A.K.M.Naim Ishtiaq, Shariful Islam, Md. Rasel Rana, Md. Ashraf Ali, Karimul Hoque, Prediction of new 212 M2AB2 borides as a promising candidate for future engineering: DFT calculations, Mater. Today Commun. 39 (2024) 108536.
[65] Xiao-Hong Li, Hong-Ling Cui, Rui-Zhou Zhang, Structural, optical, and thermal properties of MAX-phase Cr 2 AlB 2, Front. Phys. 13 (2018) 1–9.
[66] Woochul Kim, Strategies for engineering phonon transport in thermoelectrics, J. Mater. Chem. C. 3 (40) (2015) 10336–10348.
[67] M.I. Naher, S.H. Naqib, An ab-initio study on structural, elastic, electronic, bonding, thermal, and optical properties of topological Weyl semimetal Ta X (X= P, As), Sci. Rep. 11 (1) (2021) 5592.
[68] Frantsevich, Ivan Nikitich. "Elastic constants and elastic moduli of metals and insulators." Reference book (1982).
[69] S.F. Pugh, XCII. Relations between the elastic moduli and the plastic properties of polycrystalline pure metals, Lond., Edinb., Dublin Philos. Mag. J. Sci. 45 (367) (1954) 823–843.
[70] W.R.L. Lambrecht, B. Segall, Michael Methfessel, M. Van Schilfgaarde, Calculated elastic constants and deformation potentials of cubic SiC, Phys. Rev. B 44 (8) (1991) 3685.
[71] Zhigang Wu, Xiao-Jia Chen, Viktor V. Struzhkin, Ronald E. Cohen, Trends in elasticity and electronic structure of transition-metal nitrides and carbides from first principles, Phys. Rev. B—Condens. Matter Mater. Phys. 71 (21) (2005) 214103.
[72] Fangzhi Li, Bin Liu, Jingyang Wang, Yanchun Zhou, Hf3AlN: a novel layered ternary ceramic with excellent damage tolerance, J. Am. Ceram. Soc. 93 (1) (2010) 228–234.
[73] Orson L. Anderson, Harold H. Demarest Jr., Elastic constants of the central force model for cubic structures: Polycrystalline aggregates and instabilities, J. Geophys. Res. 76 (5) (1971) 1349–1369.
[74] Andreas Savin, Heinz-J.ürgen Flad, J.ürgen Flad, Heinzwerner Preuss, Hans Georg von Schnering, Zur Bindung in Carbosilanen, Angew. Chem. 104 (2) (1992) 185–186.
[75] C. Donnet, A. Erdemir, Solid lubricant coatings: recent developments and future trends, Tribology Lett. 17 (3) (2004) 389–397.
[76] Hassel Ledbetter, Albert Migliori, A general elastic-anisotropy measure, J. Appl. Phys. 100 (6) (2006).
[77] A. Gherriche, A. Bouhemadou, Y. Al-Douri, S. Bin-Omran, R. Khenata, M.A. Hadi, Ab initio exploration of the structural, elastic, electronic and optical properties of a new layered perovskite-type oxyfluoride: CsSrNb2O6F, Mater. Sci. Semicond. Process. 131 (2021) 105890.
[78] Shivakumar I. Ranganathan, Martin Ostoja-Starzewski, Universal elastic anisotropy index, Phys. Rev. Lett. 101 (5) (2008) 055504.
[79] M.A. Hadi, New ternary nanolaminated carbide Mo2Ga2C: A first-principles comparison with the MAX phase counterpart Mo2GaC, Comput. Mater. Sci. 117 (2016) 422–427.
[80] M.A. Ali, M.M. Hossain, M.M. Uddin, A.K.M.A. Islam, S.H. Naqib, Understanding the improvement of thermo-mechanical and optical properties of 212 MAX phase borides Zr2AB2 (A= In, Tl), J. Mater. Res. Technol. 15 (2021) 2227–2241.
[81] M.A. Ali, M.M. Hossain, M.M. Uddin, A.K.M.A. Islam, D. Jana, S.H. Naqib, DFT insights into new B-containing 212 MAX phases: Hf2AB2 (A= In, Sn), J. Alloy. Compd. 860 (2021) 158408.
[82] M.A. Ali, Md. Mukter Hossain, A.K.M.A. Islam, S.H. Naqib, Ternary boride Hf3PB4: insights into the physical properties of the hardest possible boride MAX phase, J. Alloy. Compd. 857 (2021) 158264.

[83] Romain Gaillac, Pluton Pullumbi, François-Xavier Coudert, ELATE: an open-source online application for analysis and visualization of elastic tensors, J. Phys.: Condens. Matter 28 (27) (2016) 275201.
[84] Md Roknuzzaman, M.A. Hadi, M.A. Ali, M.M. Hossain, N. Jahan, M.M. Uddin, J. A. Alarco, Ken Ostrikov, First hafnium-based MAX phase in the 312 family, Hf3AlC2: a first-principles study, J. Alloy. Compd. 727 (2017) 616–626.
[85] Arpon Chakraborty, M.N.H. Liton, M.S.I. Sarker, M.M. Rahman, M.K.R. Khan, A comprehensive DFT evaluation of catalytic and optoelectronic properties of BaTiO3 polymorphs, Phys. B: Condens. Matter 648 (2023) 414418.
[86] Dmitry Vladimirovich Suetin, Igor Rolenovich Shein, Electronic Structure, Mechanical and Dynamical Stability of Hexagonal Subcarbides M 2C (M= Tc, Ru, Rh, Pd, Re, Os, Ir, and Pt): Ab Initio Calculations, Phys. Solid State 60 (2018) 213–224.
[87] Orson L. Anderson, A simplified method for calculating the Debye temperature from elastic constants, J. Phys. Chem. Solids 24 (7) (1963) 909–917.
[88] David R. Clarke, Simon R. Phillpot, Thermal barrier coating materials, Mater. Today 8 (6) (2005) 22–29.
[89] Yuchen Liu, Valentino R. Cooper, Banghui Wang, Huimin Xiang, Qian Li, Yanfeng Gao, Jiong Yang, Yanchun Zhou, Bin Liu, Discovery of AB O3 Perovskites as Thermal Barrier Coatings through High-Throughput First Principles Calculations, Mater. Res. Lett. 7 (4) (2019) 145–151.
[90] Kunpeng Zhao, Chenxi Zhu, Pengfei Qiu, Anders B. Blichfeld, Espen Eikeland, Dudi Ren, Bo.B. Iversen, Fangfang Xu, Xun Shi, Lidong Chen, High thermoelectric performance and low thermal conductivity in Cu2− yS1/3Se1/3Te1/3 liquid-like materials with nanoscale mosaic structures, Nano Energy 42 (2017) 43–50.
[91] Edward Dechaumphai, Dylan Lu, Jimmy J. Kan, Jaeyun Moon, Eric E. Fullerton, Zhaowei Liu, Renkun Chen, Ultralow thermal conductivity of multilayers with highly dissimilar debye temperatures, Nano Lett. 14 (5) (2014) 2448–2455.
[92] Rahman, Md. Atikur, Mst Asma Khatun, Md. Hasan Mia, Mst Zugrufa, and Ahmad Irfan. "First-Principles Calculations to Investigate the Structural, Mechanical, Electronic, Optical and Thermal Properties of Disilicides Materials UT2Si2 (T= Ru, Rh, and Pd)." physica status solidi (b): 2400230.
[93] Mst A. Khatun, M.H. Mia, M.A. Hossain, F. Parvin, A.K.M.A. Islam, The Optical and thermoelectric properties of layer structured Ba2XS4 (X= Zr, Hf) for energy harvesting applications, J. Phys. Chem. Solids (2024) 112381.
[94] M.I. Naher, M. Mahamudujjaman, A. Tasnim, R.S. Islam, S.H. Naqib, AbstAb-initio insights into the elastic, bonding, phonon, optoelectronic and thermophysical properties of SnTaS2, Solid State Sci. 131 (2022) 106947.
[95] Andreas Thore, Martin Dahlqvist, Bjrn Alling, Johanna RosÈn, First-principles calculations of the electronic, vibrational, and elastic properties of the magnetic laminate Mn2GaC, J. Appl. Phys. 116 (10) (2014).
[96] M.A. Hadi, N. Kelaidis, S.H. Naqib, A.K.M.A. Islam, A. Chroneos, R.V. Vovk, Insights into the physical properties of a new 211 MAX phase Nb2CuC, J. Phys. Chem. Solids 149 (2021) 109759.
[97] Muhammad Waqas Qureshi, Xinxin Ma, Guangze Tang, Ramesh Paudel, Structural stability, electronic, mechanical, phonon, and thermodynamic properties of the M2GaC (M= Zr, Hf) max phase: an AB initio calculation, Materials 13 (22) (2020) 5148.
[98] Vincent Mauchamp, Wenbo Yu, Loik Gence, Luc Piraux, Thierry Cabioc'h, V.é ronique Gauthier, Per Eklund, Sylvain Dubois, Anisotropy of the resistivity and charge-carrier sign in nanolaminated Ti 2 AlC: Experiment and ab initio calculations, Phys. Rev. B 87 (23) (2013) 235105.
[99] Yefei Li, Yimin Gao, Bing Xiao, Ting Min, Zijian Fan, Shengqiang Ma, Leilei Xu, Theoretical study on the stability, elasticity, hardness and electronic structures of W–C binary compounds, J. Alloy. Compd. 502 (1) (2010) 28–37.
[100] T. Hong, T.J. Watson-Yang, A.J. Freeman, T. Oguchi, Jian-hua Xu, Crystal structure, phase stability, and electronic structure of Ti-Al intermetallics: TiAl 3, Phys. Rev. B 41 (18) (1990) 12462.
[101] J.-H. Xu, T. Oguchi, A.J. Freeman, Solid-solution strengthening: substitution of V in Ni 3 Al and structural stability of Ni 3 (Al, V), Phys. Rev. B 36 (8) (1987) 4186.
[102] S. Li, M.W. Rajeev Ahuja, Barsoum, Puru Jena, and Börje Johansson. "optical properties of Ti3SiC2 and Ti4AlN3, Appl. Phys. Lett. 92 22 (2008).
[103] R. Saniz, Lin-Hui Ye, Tatsuya Shishidou, A.J. Freeman, Structural, electronic, and optical properties of NiAl 3: first-principles calculations, Phys. Rev. B—Condens. Matter Mater. Phys. 74 (1) (2006) 014209.
[104] A.K.M.Naim Ishtiaq, Md. Nasir Uddin, Noor Afsary, Md. Koushik Alam, Shariful Islam, Md. Omar Faruk Rasel, Md. Ashraf Ali, Karimul Hoque, First-principles study of electronic, mechanical, and optical properties of M3GaB2 (M= Ti, Hf) MAX phases, Heliyon 10 (13) (2024).
[105] M.R. Rana, S. Islam, K. Hoque, S. Mahmud, M.A. Ali, Newly synthesized Pb-based 312 MAX phases M3PbC2 (M= Zr and Hf): A First-principles study, Diam. Relat. Mater. (2024) 111245.
[106] Martin T. Dove, Introduction to lattice dynamics, Cambridge university press, 1993.